

A  
Numerical Investigation of Augmented Heat Transfer in Rectan-  
gular Ducts with Ribs

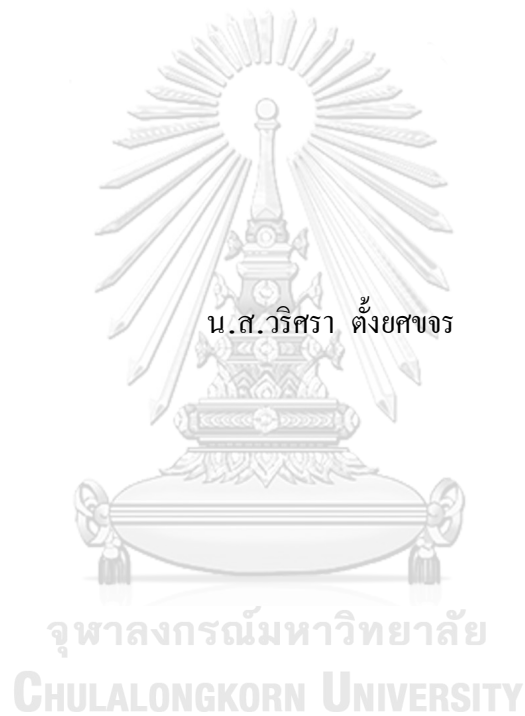


Miss Warissara Tangyotkhajorn

จุฬาลงกรณ์มหาวิทยาลัย  
CHULALONGKORN UNIVERSITY

A Thesis Submitted in Partial Fulfillment of the Requirements  
for the Degree of Master of Engineering in Mechanical Engineering  
Department of Mechanical Engineering  
Faculty of Engineering  
Chulalongkorn University  
Academic Year 2018  
Copyright of Chulalongkorn University

การศึกษาเชิงตัวเลขสำหรับการเพิ่มอัตราการถ่ายเทความร้อนในท่อสี่เหลี่ยมผืนผ้าที่มีสิ่งกีดขวาง



วิทยานิพนธ์นี้เป็นส่วนหนึ่งของการศึกษาตามหลักสูตรปริญญาวิศวกรรมศาสตรมหาบัณฑิต

สาขาวิชาวิศวกรรมเครื่องกล ภาควิชาวิศวกรรมเครื่องกล

คณะวิศวกรรมศาสตร์ จุฬาลงกรณ์มหาวิทยาลัย

ปีการศึกษา 2561

ลิขสิทธิ์ของจุฬาลงกรณ์มหาวิทยาลัย

Thesis Title	A Numerical Investigation of Augmented Heat Transfer in Rectangular Ducts with Ribs
By	Miss Warissara Tangyotkhajorn
Field of Study	Mechanical Engineering
Thesis Advisor	Assistant Professor Sompong Putivisutisak, Ph.D.
Thesis Co Advisor	Professor Suttichai Assabumrungrat, Ph.D.

---

Accepted by the Faculty of Engineering, Chulalongkorn University in  
Partial Fulfillment of the Requirement for the Master of Engineering

..... Dean of the Faculty of  
Engineering  
(Associate Professor SUPOT  
TEACHAVORASINSKUN, Ph.D.)

THESIS COMMITTEE

..... Chairman  
(Associate Professor Asi Bunyajitradulya, Ph.D.)  
..... Thesis Advisor  
(Assistant Professor Sompong Putivisutisak, Ph.D.)  
..... Thesis Co-Advisor  
(Professor Suttichai Assabumrungrat, Ph.D.)  
..... External Examiner  
(Associate Professor Pongtorn Charunyakorn, Ph.D.)

จุฬาลงกรณ์มหาวิทยาลัย  
CHULALONGKORN UNIVERSITY

วริศรา ตัญยศขจร : การศึกษาเชิงตัวเลขสำหรับการเพิ่มอัตราการถ่ายเทความร้อนในท่อ  
สี่เหลี่ยมผืนผ้าที่มีสิ่งกีดขวาง . ( A

**Numerical Investigation of Augmented Heat Transfer in Rectan-  
gular Ducts with Ribs)** อ.ที่ปรึกษาหลัก : ผศ. ดร.สมพงษ์ พุทธิวิสุทธิศักดิ์, อ.ที่  
ปรึกษาร่วม : ศ. ดร.สุทธิชัย อัสตะบำรุงรัตน์

การประยุกต์ใช้โครงสร้างขรุขระ (roughness structure) ในรูปของริบ (rib) ภายในท่อผิวเรียบเป็นวิธีหนึ่งที่มีประสิทธิภาพในการเพิ่มการถ่ายเทความร้อน แต่ส่งผลให้ความดันตกมีค่าสูงขึ้น โดยงานวิจัยนี้ได้เสนอวี-ริบ (V-rib) รูปแบบใหม่ที่มีก้านแขนงและได้ใช้การจำลองเชิงตัวเลขเพื่อศึกษาผลที่เกิดขึ้นต่อประสิทธิภาพการถ่ายเทความร้อนและความดันตก โดยมีพารามิเตอร์ที่พิจารณาคือจำนวนก้านแขนง (branching number) และอัตราส่วนพิทช์ (pitch ratio) ของวี-ริบ ผลการวิจัยแสดงให้เห็นว่าการปรับค่าสัดส่วนพิทช์ของวี-ริบมีผลกระทบต่อสมรรถนะการถ่ายเทความร้อน ในขณะที่การเปลี่ยนแปลงจำนวนก้านแขนงส่งผลต่อประสิทธิภาพการถ่ายเทความร้อนในบริเวณรอบสิ่งกีดขวางเมื่อสัดส่วนพิทช์มีค่าต่ำเท่านั้น สำหรับท่อที่มีวี-ริบในสัดส่วนพิทช์ที่สูง จำนวนก้านแขนงที่สูงจะช่วยให้ความดันภายในท่อไม่สูงเท่ากับเมื่อใส่วี-ริบที่มีจำนวนก้านแขนงต่ำ ค่าเหมาะสมที่สุดคือวี-ริบที่มี 6 ก้านและสัดส่วนพิทช์เท่ากับ 15 ซึ่งจะให้ค่าเลขนัสเซิลด์ (Nusselt number) ค่าสัมประสิทธิ์ความเสียดทาน (friction factor) และสมรรถนะเชิงความร้อน (thermal hydraulic performance) ของท่อที่มีสิ่งกีดขวางแบบวี-ริบมีค่าเป็น 2.08 เท่า 2.54 เท่า และ 1.39 เท่า ของท่อผิวเรียบ ตามลำดับ



สาขาวิชา      วิศวกรรมเครื่องกล

ลายมือชื่อนิสิต

ปีการศึกษา      2561

.....  
ลายมือชื่อ อ.ที่ปรึกษาหลัก

.....  
ลายมือชื่อ อ.ที่ปรึกษาร่วม

.....

# # 5870421121 : MAJOR MECHANICAL ENGINEERING

KEYWORDS V-ribs, Longitudinal Vortex, Branching number, Heat transfer enhancement, Pressure drop, Heat exchanger

Warissara Tangyotkhajorn : A  
 Numerical Investigation of Augmented Heat Transfer in Rectangular Ducts with Ribs. Advisor: Asst. Prof. Sompong Putivisutisak, Ph.D. Co-advisor: Prof. Suttichai Assabumrungrat, Ph.D.

The application of roughness structure of ribs inside a smooth channel is one effective way of heat transfer augmentation, but the accompanied pressure drop could be high. A novel V-rib design with branches was introduced and numerical simulations on the thermo-fluid impact of heat transfer and pressure drop were investigated. The parameters of investigation include the branching number and the pitch ratio of the V-ribs. It appears that increasing the relative pitch ratio serves to improve the overall performance of a roughened channel. The effect of the branching number is only experienced at low pitch ratio. At high pitch ratio, varying the branching number only serves to lower the pressure drops. Optimization was found at the branching number of 6 and the relative pitch ratio of 15. At optimal conditions, the Nusselt number ratio, friction factor ratios, and the thermohydraulic performance were 2.15, 2.85, and 1.39 times the plane channel, respectively.

จุฬาลงกรณ์มหาวิทยาลัย  
 CHULALONGKORN UNIVERSITY

Field of Study: Mechanical Engineering  
 Academic Year: 2018

Student's Signature  
 .....  
 Advisor's Signature  
 .....  
 Co-advisor's Signature  
 .....

## ACKNOWLEDGEMENTS

Above all else, I acknowledge my God, who so loved me in guiding me into this degree and allowed me to remain to the very end. He has given me joy in being able to do physics, mathematics, and be able to see where it can be useful even to the slightest. Unto Him with this degree, may His name forever be praised.

Secondly, I acknowledge and give thanks to my main advisor, Asst. Prof. Sompong Putivisutisak, who endured a difficult task in walking along side me throughout the course of my thesis work to which I greatly struggled with the old topic that I did not complete. You have given me much room of freedom to explore a chosen area of research, which is exactly what I need. I do appreciate you listening to me weekly and directing me. Thank you so much, sir.

Thirdly, I acknowledge and give thanks to my co-advisor, Prof. Suttichai Assabumrungrat, for his kind encouragements and guidance.

Fourthly, I would like to acknowledge Kanin Mongkol, a lab friend, who has been kind in teaching me the arts of SolidWorks as well as answering questions related to computational works.

Fifth, I give special thanks to Ruth Duffin, a sister in Christ, who has been such a gift to me in caring for me personally.

Lastly, I give thanks to the Lord for mom, dad, and my siblings. You are the reason for this degree and so with the time I have spent, I have loved you.

Warissara Tangyotkhajorn

# TABLE OF CONTENTS

	<b>Page</b>
.....	iii
ABSTRACT (THAI) .....	iii
.....	iv
ABSTRACT (ENGLISH) .....	iv
ACKNOWLEDGEMENTS .....	v
TABLE OF CONTENTS .....	vi
List of Tables .....	viii
List of Figures .....	ix
CHAPTER 1 INTRODUCTION .....	1
1.1 Background and Motivation .....	1
1.1.1 Ribs .....	2
1.1.2 Transverse ribs .....	3
1.1.3 Inclined rib and V-ribs .....	1
1.1.4 Discrete ribs: transverse, inclined, V-ribs. ....	4
1.1.5 V-ribs with groove, protrusion, and dimple. ....	9
1.1.6 Multi V-ribs .....	10
1.1.7 Arc-ribs .....	12
1.2 Objectives .....	14
1.3 Significance of the work .....	15
1.4 Scope of the research .....	16
CHAPTER 2 HEAT TRANSFER AND FRICTIONAL LOSS .....	18
2.1 Theory of Heat Transfer .....	18
2.2 Concept of Frictional Loss .....	21
2.3 Thermal Hydraulic Performance .....	22
CHAPTER 3 NUMERICAL METHODS .....	23

3.1 Turbulence model and solver in ANSYS 18 .....	23
3.2 Assumptions .....	23
3.3 Governing Equation.....	24
3.4 Boundary conditions .....	25
3.5 Solver.....	26
3.6 Turbulence Model.....	27
CHAPTER 4 RESULTS AND DISCUSSION .....	32
4.1 Numerical validation with experiments .....	32
4.3 The Thermal Hydraulic Interpretation.....	36
4.3.1 Effects of the Reynolds number .....	36
4.3.2 Effects of pitch ratio .....	41
4.3.3 Effects of the branching number .....	45
4.4 The Physics Insight.....	49
4.4.1 Streamline and velocity vector .....	49
4.4.2 Vorticity contour .....	54
4.4.3 Pressure contours .....	56
4.4.4 Nusselt number contours .....	58
CHAPTER 5 CONCLUSION AND SUGGESTION FOR FUTURE WORKS .....	1
5.1 Conclusion .....	1
5.2 Suggestion for future works.....	2
REFERENCES .....	3
VITA.....	8



## List of Tables

Table 1. 1 Researches involving transversal ribs of different cross-sectional shapes ...	4
Table 1. 2 Researches involving continuous ribs with different angle of inclinations ..	3
Table 1. 3 Researches with discrete ribs of different angle of inclinations .....	7
Table 1. 4 Research of v-ribs with grooves, dimples, and protrusion. ....	9
Table 1. 5 Researches with multi v-ribs or w-ribs .....	11
Table 1. 6 Researches pertain arc-rib.....	13
Table 1. 7 Parameters of study.....	16
Table 1. 8 Geometry of the Channel.....	16
Table 1. 9 Rib's Geometry .....	16
Table 1. 10 Fluid properties .....	16
Table 1. 11 Case studies.....	17
Table 3. 1 Solver available in ANSYS 18 [40].....	26
Table 3. 2 Segregated numerical schemes in ANSYS [40] .....	26
Table 3. 3 Turbulence model offers in ANSYS 18 [40]. ....	27
Table 3. 4 The turbulence viscosity for different $k - \omega$ formulations [40].....	29
Table 3. 5 Turbulence Prandtl number for $k$ and $\omega$ [40].....	29
Table 3. 6 The generation of specific dissipation rate $\omega$ [40].....	30
Table 3. 7 The dissipation of turbulence kinetic energy, $k$ [40]. ....	30
Table 3. 8 The dissipation of specific dissipation rate $\omega$ [40]. ....	31
Table 3. 9 Spatial discretization offers in ANSYS 18 [40]. ....	31

## List of Figures

Figure 1. 1 Flow Separation.....	2
Figure 1. 2 Nusselt number contour and secondary flows induced by inclined and V-ribs placed staggered on opposite walls. ....	1
Figure 1. 3 Iso-Nusselt number contour [24].....	5
Figure 1. 4 Top view of the branched continuous v-down ribs .....	15
Figure 1. 5 Schematic diagram of the internal of the solar receiver .....	17
Figure 2. 1 Heating plate and thermocouple positions in the experiment [8]. ....	19
Figure 2. 2 Positions of local temperature. ....	20
Figure 2. 3 Position for the inlet and outlet pressure. ....	21
Figure 4. 1 Mesh of smooth channel      Figure 4. 2 Mesh of channel with ribs .....	32
Figure 4. 3 Validation with experiment [8] for a smooth channel. ....	33
Figure 4. 4 Validation with experiment [8] for a channel with ribs. ....	34
Figure 4. 5 Nusselt number and friction factor for the smooth channel for this simulation.....	35
Figure 4. 6 Nu vs. Re .....	36
Figure 4. 7 f vs. Re .....	37
Figure 4. 8 Thermal hydraulic performance vs. Re .....	39
Figure 4. 9 THP vs. Re at various the optimal $P/e$ for specific $B$ . ....	40
Figure 4. 10 Nu/Nuo vs. $P/e$ .....	41
Figure 4. 11 $f/f_0$ vs. $P/e$ .....	42
Figure 4. 12 Effects of the relative pitch ratio on heat transfer and pressure drop at different $B$ . ....	44
Figure 4. 13 Effects of the branching number on heat transfer and frictional loss .....	45
Figure 4. 14 Effects of branching number on thermal hydraulic performance .....	47
Figure 4. 15 Front View of Streamline .....	49
Figure 4. 16 Front view of velocity vector ( $x=0.55\text{m}$ ) .....	50
Figure 4. 17 Top view of the velocity vector .....	51
Figure 4. 18 Sideview of the velocity vector (left) and sideview of the streamline (right) .....	52

Figure 4. 19 Top view of the vorticity contour for $P/e=20$ and $Re=86500$ . ....	54
Figure 4. 20 Pressure contour for $P/e=20$ and $Re=86500$ . ....	56
Figure 4. 21 Nusselt number contours for $P/e=20$ and $Re=86500$ . ....	58



# CHAPTER 1

## INTRODUCTION

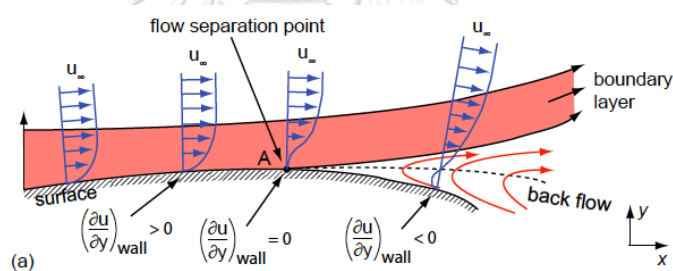
### 1.1 Background and Motivation

Heat exchanger, which transfers heat across mediums, has far-ranging applications including solar air heater [1-4], aircraft engine [5], rocket engine [6], gas turbine, electronic cooling [7], condensers, steam condensers, nuclear reactor heat exchangers [8], and even in process drying of crops, timber and fruits [9]. The thermal efficiency of the heat exchanger is dependent on the useful heat gain by the collecting fluid. For a typical smooth channel heat exchanger, this efficiency is bounded at 20% [10-13] due to the low value of the heat transfer coefficient. In such a system, the heat transfer rate is low and much heat is bestowed to the surrounding instead of being available to do useful work [2]. The cause of this high thermal resistance to heat transfer is believed to be the thick laminar boundary layer developed inside a smooth heat exchanger channel.

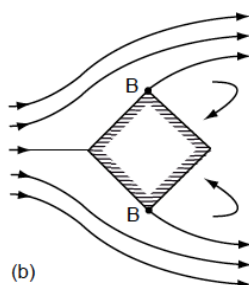
The progression of passive heat transfer enhancement techniques has been directed towards the methodology of flow perturbation via internally shaped channel into irregular patterns. Some examples of artificial roughness that are commonly applied on the underside of the heated plate include the applications of ribs, grooves, dimples, winglets, baffles, twisted tapes, and mesh wire, etc. These passive techniques improve convective heat transfer rate at minimum cost of power consumption. This is achieved by creating and intensifying turbulence near the heated wall [3, 14]. Nevertheless, as the roughened elements are turbulence promoters, they contribute a negative feedback on the incurred frictional loss. This will in turn lead to a high pumping power consumption [15, 16]. A roughness design that allows turbulence generation while mitigating frictional loss is thus a research challenge on the topic of the application of artificial roughness in heat transfer augmentation.

### 1.1.1 Ribs

Ribs or turbulators are obstructions in the heat exchanger channel that serve to redirect the flow path and disturb the viscous and thermal boundary layer [17] via phenomena such as flow separation, reattachment, recirculation, and secondary flows generation [18]. Flow separation is an important phenomenon in triggering turbulence and starting the heat transfer augmentation process [19]. Flow separation can be achieved either by smoothness of surface that incur adverse pressure gradient as shown in Figure 1.1 (a) or the sharpness of edges that physically separates the flow as in Figure 1.1 (b). This process is followed by impingements and vortex generation near the rib's vicinity. Turbulence improves momentum exchange between fast bulk stream and near wall fluid, thereby augments heat transfer. Different rib structures have shown to result in different flow characteristics with varied heat transfer enhancement effects.



(a) Pressure-based flow separation [19]



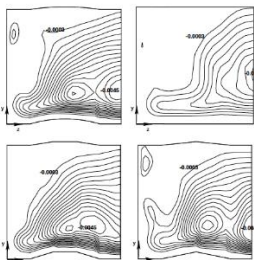
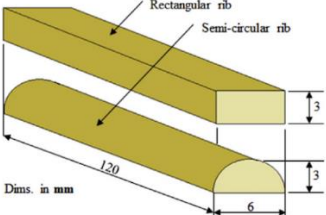
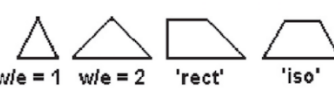
(b) Geometrical-based flow separation [19]

Figure 1. 1 Flow Separation

### 1.1.2 Transverse ribs

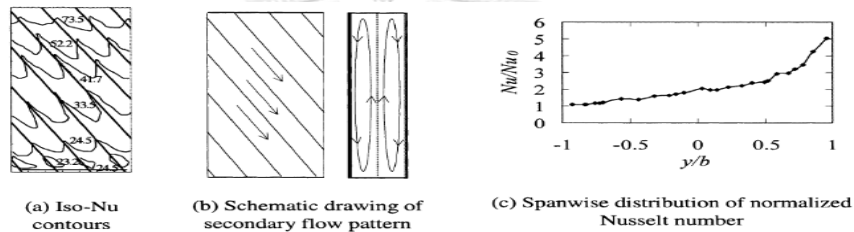
Table 1.1 displays the simplest rib type of the transverse ribs with different cross-sectional geometries including trapezoidal [6, 20], semi-circular [6, 8], triangular [6, 20], rectangular [8], and rectangular trapezoidal shapes [20]. The simulations of Vazquez et al. [6] in examining the heat transfer performance of trapezoidal, semi-circular, and triangular transverse ribs demonstrated that all transverse ribs generated vortices immediately upstream and downstream to the ribs, but these vortices were stagnant since the vortex were confined within the rib vicinity. Different cross-sectional shapes altered the vorticity strength in the recirculation zones. For example, trapezoidal rib had 1.8% of the maximal velocity strength near the rib ( $1.8\%U$ ), semi-circular rib had 1.3%, and triangular rib had 1.0%. The experiments of Alfarawi et al. [8] analyzed the Nusselt number ratio of the rectangular, semi-circular transverse ribs, and their hybrids to be in the range of 1.32-2.12, 1.22-2.00, and 1.42-2.22, respectively; corresponding with the friction factor ratios of 3.56-4.125, 3.50-4.18, and 3.56-4.125, respectively. It appeared that trapezoidal and rectangular cross-section were superior to semi-circular or triangular shapes. Out of this progression, Andreozzi et al.'s [20] experimented that triangular ribs can outpace both rectangular-trapezoidal ribs and isosceles-trapezoidal ribs in their heat transfer capacity with their Nusselt number ratios ranging between 1.42-2.22, 1.32-2.12, and 1.22-2.00, respectively; the friction factor ratios ranging between 3.56-4.125, 3.50-4.18, and 3.38-3.81, respectively; and the hydraulic performance factors ranging between 0.93-1.38, 0.87-1.32, and 0.81-1.28, respectively. The negative feedback of high pressure drops during heat transfer augmentation by transverse ribs yielded an overall low thermal hydraulic performance.

Table 1. 1 Researches involving transversal ribs of different cross-sectional shapes

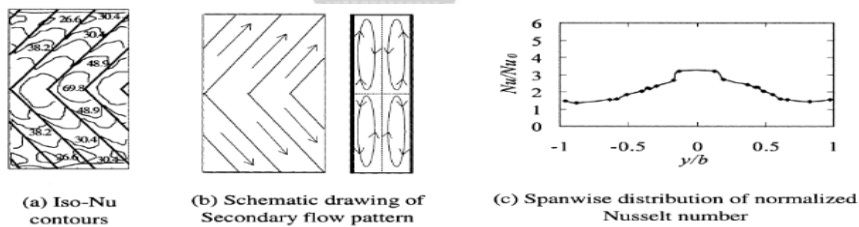
Investigators	Roughness Parameters	Roughness Geometries	Heat Transfer Enhancement	Frictional loss
Vázquez et al. [6]	Re: 6000	 <p>Outcome: Trapezoidal &gt; Circular &gt; Triangular</p>	Max Transversal Velocity (BSF),(SSF): 3.2% $U_b$ , 1.8% $U_b$ 3.0% $U_b$ , 1.3% $U_b$ 3.2% $U_b$ , 1.0% $U_b$ 1.9% $U_b$ , --	-
Alfarawi et al. [8]	Aspect ratio=4 D=64mm, L=80 0mm Re: 12,500-86,500 Hybrid:	 <p>Outcome: Hybrid &gt; Rectangular &gt; Semi-Circular</p>	Nu/Nu0: 1.42-2.22 1.32-2.12 1.22-2.0	f/fo: 3.56-4.125 3.5-3-4.18 3.38-3.81
Andreozzi et al. [20]	Re: 20,000-60,000 p/e=10		Nu/Nu0: (with, without nano-particle)	-
	Triangular-rib: Isosceles-trapezoid ('iso'): Rectangular-trapezoid ('rect'):		2.76, 2.25 2.56, 2.512 2.36, 2.32	

### 1.1.3 Inclined rib and V-ribs

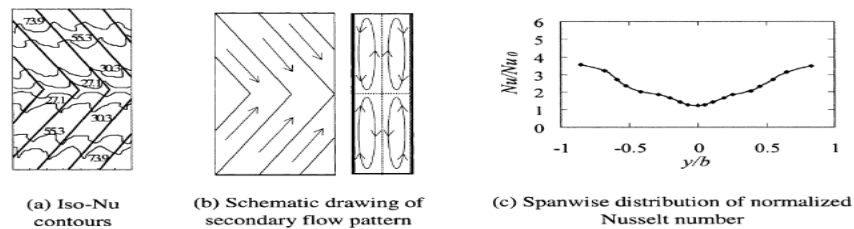
Inclining the fully transverse ribs allowed the stagnant vortices to slide along the incline, entering the leading edge and leaving at the trailing edge. Additionally, the experiments of Gao and Sunden [18] explained that inclined ribs improved heat transfer by mean of temperature gradient established along the incline, which was absent in the fully transverse. In aerodynamics, the primary stream was redirected into two cells of secondary longitudinal flows. The Nusselt number contour in Figure 1.2 (a) showed that the leading end of the incline rib augments heat transfer, while the trailing end of the rib had the Nusselt number close to the smooth channel.



(a) Iso-Nu contour and secondary pattern for inclined rib [18]



(b) Iso-Nu contour and secondary pattern for v-up rib [18]



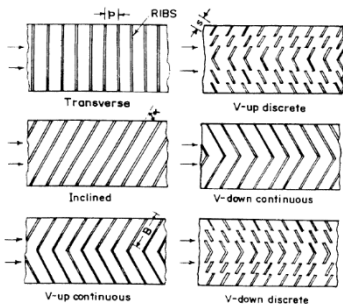
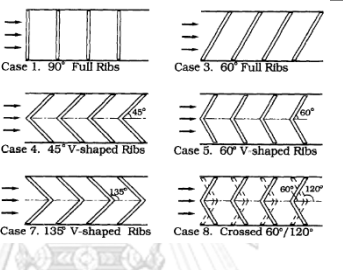
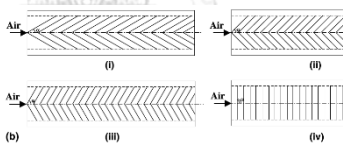
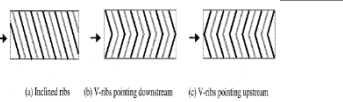
(c) Iso-Nu contour and secondary pattern for v-down rib [18]

Figure 1. 2 Nusselt number contour and secondary flows induced by inclined and V-ribs placed staggered on opposite walls.



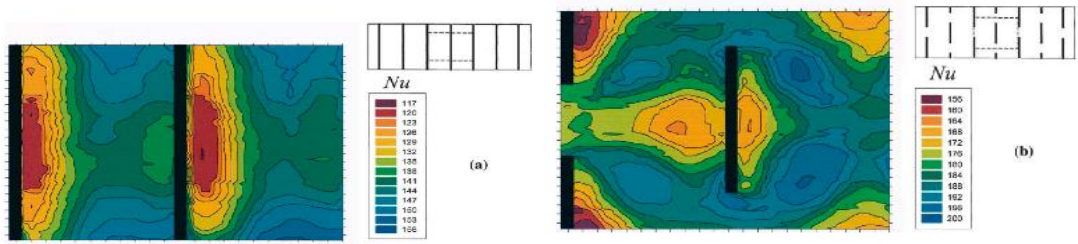
The concept of V-ribs (see Table 1.2) arose with the attempt to improve the heat transfer of inclined ribs by connecting the incline into two leading (or trailing) ends. Gao and Sunden [18] showed that V-ribs inaugurated two sources of temperature gradients together with two pairs of rotating longitudinal secondary streams. When the V-ribs were mounted on opposite walls, Figure 2 (b) revealed that the secondary cells produced by the V-rib type with the apex pointing upstream (V-up rib) were co-rotating, while in Figure 1.2 (c) V-ribs with apex pointing downstream (V-down rib) generated counter-rotating secondary flows. Although no explanation to the flow dynamics was given, Karwa et al. [21], Lau et al. [22], and Momin et al. [23] conformed that the optimal angle of inclination for V-ribs were  $60^\circ$ . At optimal angle of inclination, Karwa et al. [21] experimentally compared the continuous V-down with continuous V-up in the Reynolds range of 2800 to 15000 resulted the following Stanton number ratio range of 2.10-2.47 and 2.02-2.37, respectively. The corresponding friction factor ratio ranged between 3.32-3.65 and 3.40-3.92, respectively. The corresponding overall performance ranged between 1.41-1.60 and 1.34-2.14, respectively. The experiment of Lau et al. [22] at the Reynolds number of 15000 showed V-up and V-down at  $60^\circ$  allowed the average Stanton number ratios of 4.0 and 3.75, respectively; the corresponding friction factor ratios were 8.5 and 10.0, respectively; the corresponding thermal hydraulic performance ratios were 1.96 and 1.74, respectively. It can be seen that the heat transfer performance of V-ribs improved from the inclined; however, much heat was lost.

Table 1. 2 Researches involving continuous ribs with different angle of inclinations

Investigators	Roughness Parameters	Roughness Geometries	Heat Transfer Enhancement	Frictional loss
<b>Karwa et al. [21]</b>	Re: 2800-15,000 (transitional flow) v-down continuous rib v-down discrete rib v-up continuous rib v-up discrete rib inclined rib transverse rib		Stanton number ratio: 2.10-2.47 2.02-2.42 2.02-2.37 1.93-2.34 1.87-2.12 1.65-1.90	Friction factor ratio: 3.32-3.65 2.46-2.58 3.40-3.92 2.35-2.47 3.02-3.42 2.68-2.96
<b>Lau et al. [22]</b>	Re: 10,000-60,000 (turbulent flow) 60° v-up rib 45° v-up rib 60° v-down rib 45° v-down rib cross 60° v-rib		Stanton number ratio at Re=10 <sup>4</sup> : 1.65 1.45 1.43 1.325 1.30	Friction factor ratio at Re=10 <sup>4</sup> : 1.704 1.56 1.816 1.55 1.53
<b>Momin al. [23]</b>	Re: 2500-18,000 (transitional) Angle of inclination 90° 60° 45° 30° Relative roughness height		Nu number ratio: 1.51-2.67 1.87-2.83 1.82-2.52 1.31-2.02	Friction factor ratio: 1.30-1.50 1.51-2.17 1.75-2.05 1.23-1.37
<b>Gao et al. [18]</b>	Re:1000-6000 (laminar-transitional flow) v-up rib v-down rib	 (staggered arrangement on opposite walls)	See Figure 1.2	-

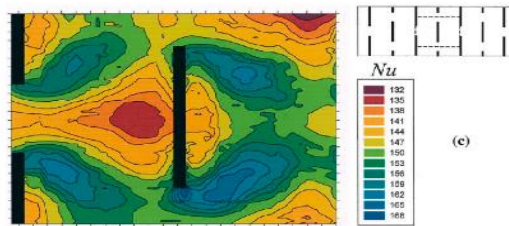
#### 1.1.4 Discrete ribs: transverse, inclined, V-ribs.

To improve the heat transfer performance of the continuous ribs, transverse [24, 25], incline [25], and V-rib [21, 24, 25] were inserted with gaps. In doing so, the flow would be accelerated at the vena contracta. Often case, stagger pieces were placed a distance away from the gap to further accelerate the flow through the gap. The experimental works of Tanda [24] shown in Figure 1.3 featured the Nusselt number contours produced by discrete transverse ribs, discrete transverse with staggered piece, and discrete V-rib with V-shaped staggered pieces. For the discrete transverse rib in Figure 1.3 (a), it can be seen that the regions of the highest heat transfer enhancement were the upstream vicinity of the rib; the zones of lowest heat transfer augmentation were the rear proximity of the ribs. By inserting the gap and the stagger piece in Figure 1.3 (b) and (c), it can be seen that the accelerated flow produced one vortex pair at the gap's tips and one more vortex pair at the stagger piece's tips. These improved mixing at local level. With the stagger piece being in V-shape as in Figure 1.3 (d)-(f), the stagnant recirculation zone in Figure 1.3 (d) at the stagger piece's rear became enlarged for high relative pitch values; for smaller relative pitch ratios in Figure 1.3 (e)-(f) the vortex pair generated by the staggered V-shape merged into one.

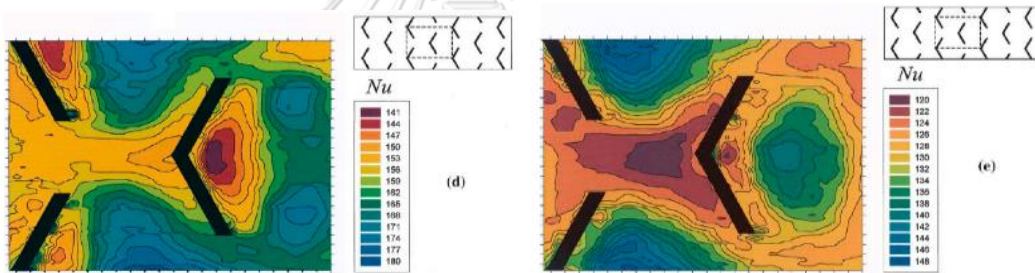


(a) transverse continuous rib

(b) transverse broken rib  $P/e=8$

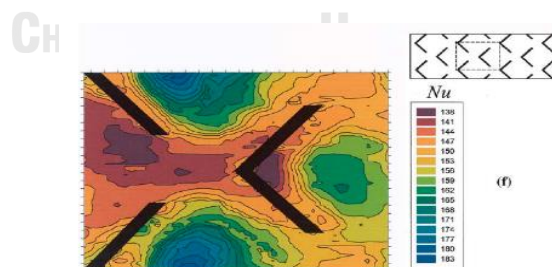


(c) transverse broken rib  $P/e=13.3$



(d) 60 v-shaped broken  $P/e=8$

(e) 60 v-shaped broken  $P/e=13.3$



(f) 45 v-shaped broken  $P/e=8$ .

Figure 1. 3 Iso-Nusselt number contour [24]

Table 1.3 contrasts the heat transfer performance of different discrete rib types. The results of Tanda [24] at the Reynolds number of 36000 showed that discrete transverse ribs with transverse staggered piece had the Nusselt number ratio of 2.20; which was higher than the discrete V-rib with 60° V-shaped staggered piece, whose the Nusselt number ratio was 1.89; followed by V-rib with 45° V-shaped staggered piece whose Nusselt number ratio was 1.48. The results of Karwa et al. [21] listed in Table 1.3 portrayed that discrete V-down was better in heat transfer performance than discrete V-up, and they both outperformed the continuous incline and transverse ribs. In the experimental results of Han and Zhang [25], also displayed in Table 1.3, the discrete V-rib with stagger pieces was better heat enhancer than those with no staggered piece, and the discrete V-rib form outpaced the discrete inclined, discrete transverse, the continuous V-shaped, continuous inclined, and transverse ribs.

Optimization on the discrete V-ribs parameters were also of research interest, see Table 1.3. Promvonge et al. [5] numerically optimized the relative rib thickness of the discrete V-ribs, where thin ribs were better than thick ribs. Singh et al. [16] also numerically optimized relative roughness pitch, angle of attack, relative gap ratio, and relative roughness height of the discrete V-ribs. The optimal rib parameters allowed the Nusselt number, friction factor, and thermal hydraulic performance of the roughened channel to be 3.04, 3.11, and 2.08 times those of a smooth channel, respectively.

Longitudinal flow arose out of inclined and V-rib shapes is an important flow characteristic in global heat transfer enhancement that directed other inclined-related or V-related creative rib models.

Table 1. 3 Researches with discrete ribs of different angle of inclinations

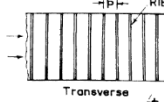
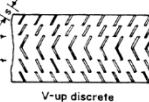
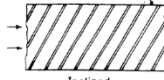



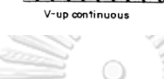
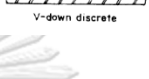


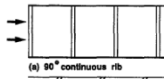
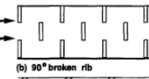
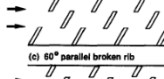

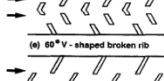
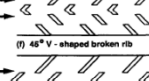
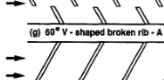
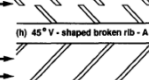
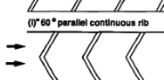
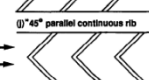
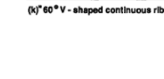
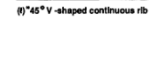

Investigators	Roughness Parameters	Roughness Geometries	Heat Transfer Enhancement	Frictional loss
Karwa et al., 2003 [21]	Re: 2800-15,000 (transitional flow) v-down continuous rib v-down discrete rib v-up continuous rib v-up discrete rib inclined rib transverse rib		Stanton number ratio: 2.10-2.47 2.02-2.42 2.02-2.37 1.93-2.34 1.87-2.12 1.65-1.90	Friction factor ratio: 3.32-3.65 2.46-2.58 3.40-3.92 2.35-2.47 3.02-3.42 2.68-2.96
				
				
				
				
				
				
				
				
				
Han and Zhang, 1991 [25]	Re: 15,000-18,000 60° v-shaped broken 60° v-shaped broken A 45° v-shaped broken A 60° inclined broken 45° v-shaped broken 45° parallel broken 90° transverse broken transverse continuous		4.2 4.0 3.8 3.6 3.6 3.55 3.3 2.45	-
				
				
				
				
				
				
				
				
				
				
				
				

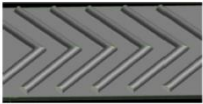
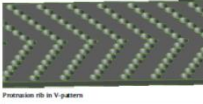


Table 1.3 Researches with discrete ribs of different angle of inclinations (continue)

Investigators	Roughness Parameters	Roughness Geometries	Heat Transfer Enhancement	Frictional loss
Promvongse et al., 2011 [5]	Re:10,000-25,000  Relative thickness ratio: $s/D=0.0125$ $s/D=0.0625$ Relative roughness height: $e/D:0.05-0.125$ (Re=10,000)		3.2-4.05 3.1-3.8	9.2-10.2 7.8-9.0
Singh et al., 2011 [16]	Re: 3000-15,000  Optimal conditions: $p/e=8.0$ , $d/w=0.65$ , $g/e=1.0$ , $\alpha=60$ , $e/D=0.043$		3.04	3.11

### 1.1.5 V-ribs with groove, protrusion, and dimple.

Kumar and Kim [26], referenced in Table 4, did a three-dimensional simulation to investigate the Nusselt number and friction factor using conventional V-pattern rib, protrusion rib in V-pattern, dimple rib in V-pattern, and V-pattern rib combined with grooves for Reynolds number ranging between 5000 to 20000. The Nusselt number ratio ranked from the highest to the lowest for the models were: 2.25-5.625 for V-pattern rib combined with grooves, 2.125-4.625 for dimple rib in V-pattern, 1.9375-4.625 for protrusion rib in V-pattern, and 1.81-4.00 for V-pattern. Their corresponding friction factors were 3.95-7.67, 3.80-7.17, 3.70-6.33, and 3.50-6.00. Grooves surface casting improved the overall performance of the V-ribs by 1.42-2.85 times the smooth channel by promoting subsidiary vortices along the inter-ribs. This observation was also found by Lorenzini-Gutierrez et al. [27]. The subsidiary streams were noteworthy flow structure to be investigated.

Table 1. 4 Research of v-ribs with grooves, dimples, and protrusion.

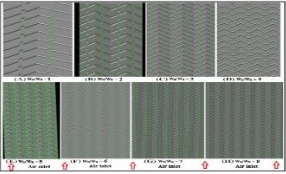
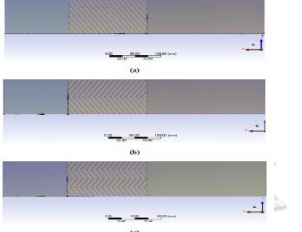
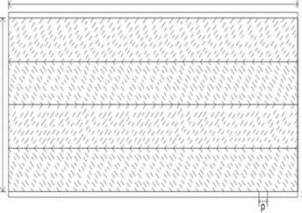
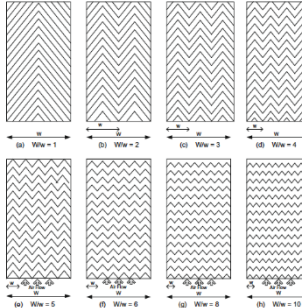
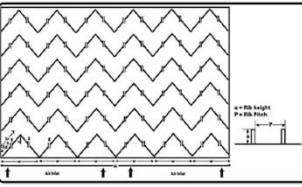

Investigators	Roughness Parameters	Roughness Geometries	Heat Transfer Enhancement	Frictional loss
<b>Kumar and Kim [26]</b>	V-pattern rib combined with grooves,		2.25-5.625	3.95-7.67,
	Dimple rib in V-pattern,		2.125-4.625	3.80-7.17,
	Protrusion rib in V-pattern		1.9375-4.625	3.70-6.33,
	V-pattern		1.81-4.00	3.50-6.00



### 1.1.6 Multi V-ribs

As the V-ribs induced secondary flows and subsidiary streams down the incline, researches on W-ribs [28, 29], M-ribs [30] and multi V-rib shapes [1, 2, 9, 10, 12] increased the serration of the V-ribs to both increase the number of sources of temperature gradient and subsidiary streams down the incline. Thakur et al. [28] numerically compared inclined ribs, V-down ribs, and W-ribs. For the Reynolds number of 15000, the respective Nusselt number ratio were 1.04 to 1.19, and 1.23; and their respective friction factors were 1.04, 1.19, and 1.23. The optimal angle of attack for the W-rib was 60°. Rohit and Lanjewar [29] experimentally considered the discrete W-up and discrete W-down ribs (Re=14000) with the comparative Nusselt number ratios of 2.35 and 2.60; and the friction factor ratios of 2.78 and 1.98, respectively. Han et al.'s [15] experimentally audited the V-rib's serration from 1-10. The optimal relative width ratio ( $W/w$ ) was the serration of 6. The Nusselt number ratio was 5.52; the friction factor ratio was 3.13 for the Reynolds number of 14000. Jin et al.'s [31] numerical work confirmed that the relative width ratio of 6 was optimal. By introducing gaps to the multi V-ribs, Kumar et al. experimentally [2, 32] found that the optimal relative width ratio was also at 6, corresponding to the Nusselt number ratios and friction factor ratios of 3.1 and 5.5, in that order, for the Reynolds number of 14000. A further annex of the stagger pieces to the gaps from the experiment of Kumar and Kim [1] raised the Nusselt number ratio up to 8.5 and the friction factor ratio to 7.1 for the Reynolds number of 16000. However, for the experiments of Ravi and Saini [9] at the Reynolds number of 14000 and relative pitch ratio of 6, these values were only 3.1 and 2.45, respectively. It can be seen that V-rib with gaps surged the Nusselt number ratio; nevertheless, the rise in frictional loss was paramount.

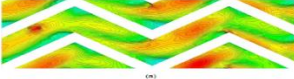
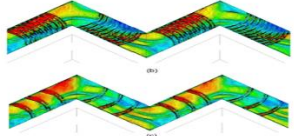
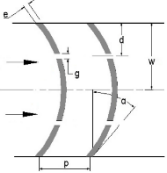
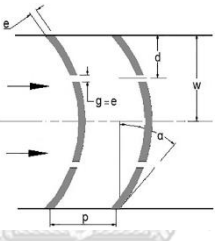
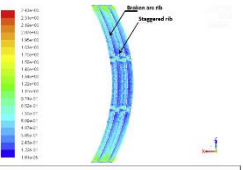
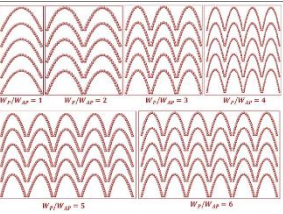
Table 1. 5 Researches with multi v-ribs or w-ribs

Investigators	Roughness Parameters	Roughness Geometries	Heat Transfer Enhancement	Frictional loss
<b>Kumar and Kim, [1]</b>	Re:4000-24,000 W/w=6		5.71-9.28	-
<b>Thakur et al. [28]</b>	Re:4000-15000 w-rib v-rib inclined		0.90-1.04, 1.10-1.19, 1.14-1.23	0.05-0.096, 0.076-0.152, 0.088-0.186
<b>Rohit et al. [29]</b>	Re:4000-14,000 W-down W-up		1.92-2.60 1.54-2.35	
<b>Hans et al. [15]</b>	Re:2000-20000 Optimal condition:  $e/D=0.043$ , $p/e=8$ , $\alpha = 60^\circ$ , $W/w=6$ .		2.50-4.88	3.33-4.00
<b>Kumar et al. [2, 32]</b>	Re:4000-20,000 $e/D=0.044$ , $W/w=6$ , $d/W=0.69$ , $g/e=1$ , $\alpha = 60^\circ$ .		6.74	6.37
<b>Ravi et al. [9]</b>	Re:2000-20000 Optimal staggered rib size: $r/e=2.5$		2.97-3.40	1.95-2.45

### 1.1.7 Arc-ribs

The latest creative design in adoption of V-rib shapes introduced centripetal acceleration along the incline by arching the V-shape into arc-rib type [25, 33-37]. From the literatures in Table 10, techniques of gaps insertion [15, 34, 36], staggered piece addition [34], serration extension [36, 37], and protrusion [36, 37] in arc-shapes were explored. The three-dimensional simulations of Lee and Kim [33] examined the thermo-hydraulic performance of continuous arc-rib in zigzag channel. The Nusselt number was augmented by 62.7% with the increased in pressure drop of 51.5% for the model A (see Table 1.6). With the insertion of gaps, Hans et al. [25] optimized the relative roughness pitch (4-12), relative gap width (0.5-2.5), relative gap position (0.2-0.8), relative roughness height (0.022-0.043), and arc angle ( $15^{\circ}$ - $75^{\circ}$ ) through experiments. The Nusselt number ratio and friction factor ratios at optimal conditions were 2.63 and 2.44 times those of a smooth duct, respectively. Gill et al. [34] confirmed the results of Han et al. [25] numerically investigating the optimal gap position of the broken arc-ribs. Gill et al. [34] further included the effects of the staggered piece at the proximity of the gap. At optimal rib's conditions and the Reynolds number of 4000, the Nusselt number and friction factor increased by 3.06 and 2.50 times those of the smooth channel, respectively. The experiments of Nadda et al. [36, 37] included both serration effects and protrusion effects into the multiple protrusion arc-ribs. At the Reynolds range of 5000 to 19000, the optimal relative width ratio was the serration of 5, corresponding to the Nusselt number ratio range of 3.64-6.29 and the friction factor ratio range of 8.33-10.5. Indeed, the Nusselt number was greatly augmented, yet the raise in friction factor ratio was also supreme.

Table 1. 6 Researches pertain arc-rib

Investigators	Roughness Parameters	Roughness Geometries	Heat Transfer Enhancement	Frictional loss
Lee and Kim, 2015 [33]	Design A		1.627	1.515
	Design B		1.594	1.059
Han et al., 2016 [25]	Re:2000-16,000 Optimal condition: $p/e=10$ , $g/e=1.0$ , $d/w=0.65$ , $e/D=0.043$ , $\alpha = 30^\circ$		2.63	2.44
Gill et al. [34]	Re:2000-16,000  Optimal relative gap position (0.2-0.8): 0.65		1.62-2.55	1.68-2.37
Gill et al. [35]	Relative staggered rib size (1-6): 4		3.06	2.50
Nadda et al. [36, 37]	Re: 5000-19,000 Optimal condition: $W_p/W_{ap}=5.0$ , $P_p/e_p=9.5$ , $e_p/d_p=1.0$ , $\alpha = 55^\circ$		3.64-6.29	8.33-10.5

The question arises, what are the rib features that induced specific flow characteristics that allowed enhancement of heat transfer? What are some possible rib features that reduce the pressure drop? The literature survey deduced the following:

1. *transverse ribs*--induced localized vortices upstream and downstream to ribs.
2. *inclined ribs*--generate longitudinal secondary flows.
3. *V-ribs*--(on opposite walls) increase the number of longitudinal secondary flow cells.
4. *discrete rib forms* --allowed acceleration through the gaps.
5. *staggered piece*--further accelerate the flow from the gaps.
6. *arc-shape*--accelerate the flow along the arc length and induced secondary flows.
7. *multiple rib type*--increase the number of subsidiary streams down the rib length.

## 1.2 Objectives

The objectives of the work are as follows:

- (i) To introduce new roughness designs for heat transfer augmentation of a heat exchanger. The designs are shown in Figure 1.4.
- (ii) To understand the effects of increasing the branching number ( $B=2, 4, 6, \text{ and } 8$ ) on the continuous V-down rib on the heat transfer and friction characteristics.
- (iii) To investigate the optimal relative pitch ratio ( $P/e=10, 12, 15, 17, 20$ ) of the newly designed rib shown in Figure 1.4.

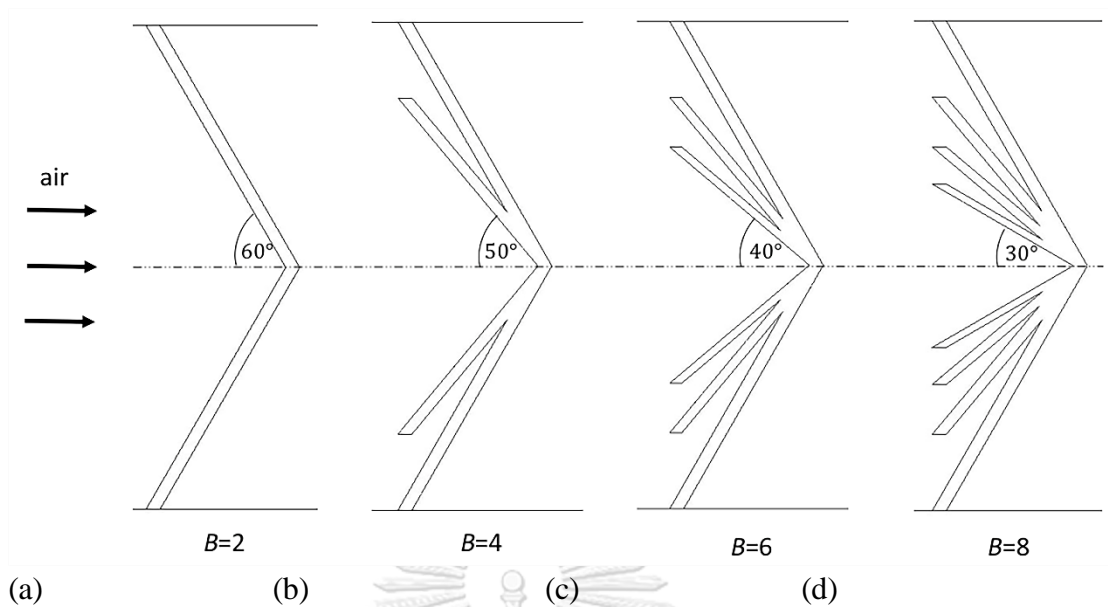


Figure 1. 4 Top view of the branched continuous v-down ribs

### 1.3 Significance of the work

The novelty of this work proves that branched V-rib is another rib type that redirects the primary stream into longitudinal secondary flows. The branched V-ribs increased the number of subsidiary streams down the incline of the branches. This improved the heat transfer augmentation of the ribbed channel, but most importantly pressure drop was reduced due to the branching effects. This is because the branches fragmented the initial surface area of contact between the fluid stream and solid-rib. There is an optimal branching number that improved the thermal hydraulic performance of the heat exchanger being  $B=6$  to which the pressure loss can be suppressed.

### 1.4 Scope of the research

Three dimensional numerical simulations will be performed using ANSYS Fluent 18.0 to explore the thermo-fluid characteristics of air in rectangular channel with ribs. The parameters investigated include the V-rib's branching number and the pitch ratio listed in Table 1.7. Fixed channel's geometries are given in Table 1.8 and fixed rib's parameters are listed in Table 1.9. Table 1.10 displays the properties of the fluid selected.

Table 1. 7 Parameters of study

Parameters varied	
Pitch, $P$ [mm]	30, 36, 42, 51, 60
Relative Pitch ratio, $P/e$	10, 12, 15, 17, 20
Branching Number, $B$	2, 4, 6, 8

Table 1. 8 Geometry of the Channel

Channel's Geometry	
Width, $W$ [mm]	120
Height, $H$ [mm]	40
Entrance length, $L_{en}$ [mm]	1900
Length of tested channel, $L_t$ [mm]	1000
Exit length, $L_{ex}$ [mm]	240
Aspect ratio, $AR$	3

Table 1. 9 Rib's Geometry

Rib's Geometry	
Pitch, $P$ [mm]	30, 36, 42, 51, 60
Rib's height and width, $e$ [mm]	3
Relative Pitch ratio, $P/e$	10, 12, 15, 17, 20
Branching Number, $B$	2, 4, 6, 8
Angle of inclination, $\theta$	30°, 40°, 50°, 60°
Number of ribs	10

Table 1. 10 Fluid properties

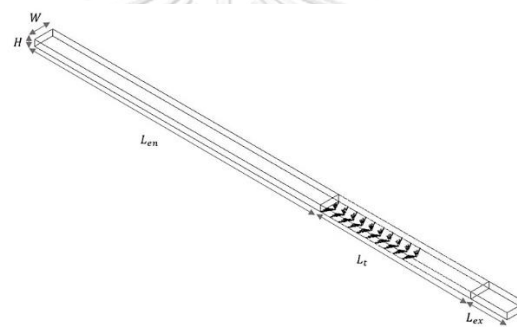
Properties of air	
Density, $\rho$ [ $kg/m^3$ ]	1.225
Dynamic viscosity, $\mu$ [ $kg/m/s$ ]	$1.7894 \times 10^{-5}$
Thermal conductivity, $k$ [ $W/m/K$ ]	0.0242

### Case studies:

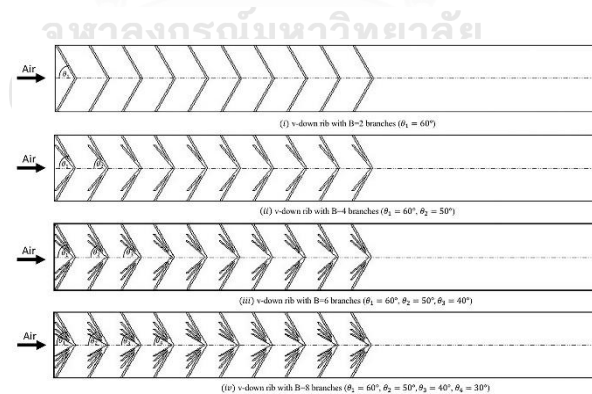
The four branched v-rib types investigated are listed below. The angles of inclination for the branched v-ribs are depicted in Figure 1.11. The ribs are only placed on the heated plate.

Table 1. 11 Case studies

Case	V-down with branching number ( $B$ )	Angle of attack present in ribs
1	2	$60^\circ$
2	4	$50^\circ, 60^\circ$
3	6	$40^\circ, 50^\circ$ and $60^\circ$
4	8	$30^\circ, 40^\circ, 50^\circ$ and $60^\circ$



(a) Over view of geometrical model



(b) Roughness elements on heated plate

Figure 1. 5 Schematic diagram of the internal of the solar receiver



## CHAPTER 2

### HEAT TRANSFER AND FRICTIONAL LOSS

#### 2.1 Theory of Heat Transfer

Heat transfer is a phenomenon near wall, where heat is conducted from the wall to fluid and convection begins. Thus, at the wall, the rate of conduction heat transfer can be said to be equal to the rate of convection heat transfer.

$$Q_{conduct} = Q_{convect} \quad (2.1)$$

where the heat of conduction,  $Q_{conduct}$  and heat of convection,  $Q_{convect}$  are defined as follows

$$Q_{conduct} = -kA \frac{\partial}{\partial y} (T - T_f)|_{y=0} \quad (2.2)$$

$$Q_{convect} = h_x A (T - T_f)|_{y=0} \quad (2.3)$$

where  $k$ ,  $A$ , and  $h_x$ , and  $T$  are the conduction heat transfer coefficient, the surface area of heat transfer, and the local convection heat transfer coefficient, and local wall temperature, respectively. From (2.1) to (2.3), the local heat transfer coefficient can be defined:

$$h_x = \frac{q''_{conduct}}{(T - T_f)} \quad (2.4)$$

where  $q''$  is the net heat flux through the heated plate. For this present work,  $q''$  is  $1110 \text{ W/m}^2$ .  $T_f$  is the average temperature of the inlet ( $T_{t,o}$ ) and the outlet ( $T_{t,L}$ ) of the tested section,

$$T_f = \frac{T_{t,o} + T_{t,L}}{2} \quad (2.5)$$

The local wall temperature,  $T$ , is obtained from the thermocouple position as shown in Figure 2.1 from the experiment of Alfarawi et al. [8].

From the local convective heat transfer coefficient, the local Nusselt number was defined based on the hydraulic diameter ( $D$ ),

$$Nu_x = \frac{h_x D}{k} \quad (2.6)$$

The average Nusselt number takes the numerical integration of the local values and divided by the characteristic length as defined by Alfarawi et al. [8],

$$Nu = \frac{\sum_{x=0}^{x=L} Nu_x}{L} \quad (2.7)$$

$$\frac{Nu}{Nu_o} = \frac{\text{average Nusselt number of roughened channel}}{\text{average Nusselt number of smooth channel}} \quad (2.8)$$

The  $Nu_o$  is the average Nusselt number of the smooth channel.

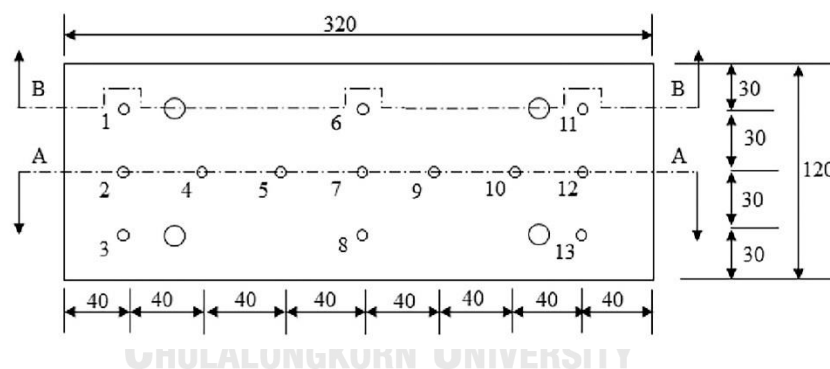
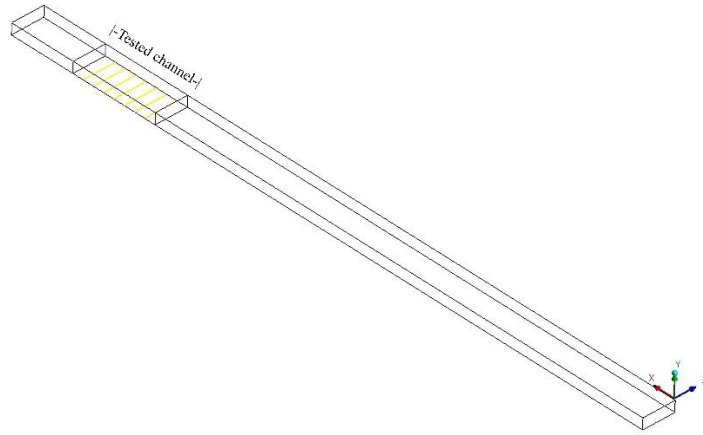
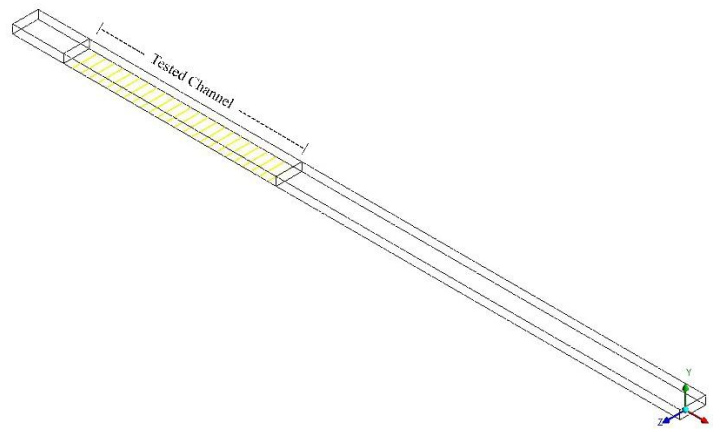


Figure 2. 1 Heating plate and thermocouple positions in the experiment [8].

Figure 2.2 (a) displays the line positions of the smooth channel in accordance with Alfarawi et al [8]. Figure 2.2 (b) displays the line position of the smooth channel for this present work. Details on how the numerical integration of the local temperature works experimentally is provided in page 136 of [8].



(a) Smooth channel for validation ( $L_t = 320$  cm).



(b) Smooth channel for present work ( $L_t = 1000$  cm).

Figure 2. 2 Positions of local temperature.

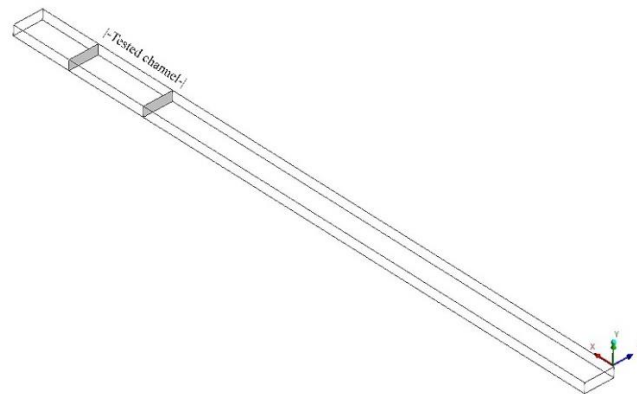
## 2.2 Concept of Frictional Loss

The frictional loss of the system is monitored via the Darcy friction factor ( $f$ ) and the friction factor ratio in Eq. 2.10 compares the friction factor of a roughened channel with those of the smooth channel.

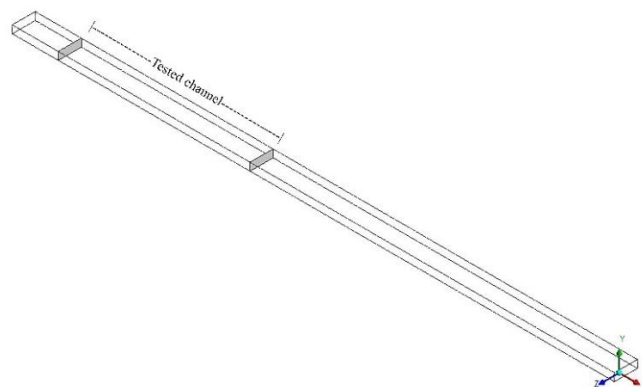
$$f = \left( \frac{\Delta P}{\frac{1}{2} \rho_f U_m^2} \right) \frac{D}{L_t} \quad (2.9)$$

$$\frac{f}{f_0} = \frac{\text{friction factor of roughened channel}}{\text{friction factor of smooth channel}} \quad (2.10)$$

where  $U_m$  is the averaged inlet velocity,  $\Delta P$  the pressure drop across the tested channel, and  $\rho_f$  is the fluid density.



(a) Smooth channel for validation ( $L_t = 320$  cm).



(b) Smooth channel for present work ( $L_t = 1000$  cm).

Figure 2. 3 Position for the inlet and outlet pressure.

Figure 2.3 (a) and (b) display the positions of measurement for the pressure drop across the tested channel for the experimental validation and for the smooth channel of the present work.

### 2.3 Thermal Hydraulic Performance

The overall performance of the channel is monitored by the thermal hydraulic performance (THP), namely:

$$\text{THP} = \frac{(\text{Nu}/\text{Nu}_0)}{(f/f_0)^{1/3}} \quad (2.11)$$



## CHAPTER 3

### NUMERICAL METHODS

#### 3.1 Turbulence model and solver in ANSYS 18

ANSYS Fluent 18.0 was used to simulate the problem of fluid flow and heat transfer in a 3-dimensional rectangular channel. The turbulent scheme employed was  $k - \omega$ , as according to [40,41] it is designed particularly for near wall calculation. Also, the SST option allows accurate onset of flow separation from the smooth surface, to which this work investigates. Additionally, the calculation from  $k - \omega$  SST scheme is robust and fast. (See Table 3.3 for comparison different turbulence models.) The pressure-velocity coupling scheme is SIMPLE. Through trials and experiments it was found that the following spatial discretization schemes allow the closest result to the experimental value of [8], namely: second order UPWIND is selected for pressure, while QUICK scheme is selected for the momentum, turbulent kinetic energy, specific dissipation rate, and energy. For more details on the solver available, the scheme to couple pressure and velocity, and spatial discretization see Table 3.1-3.2 and Table 3.9.

#### 3.2 Assumptions

The assumptions to the problem are:

- The flow and heat transfer are in steady state
- The flow is fully developed in the entrance region
- The flow is turbulent and incompressible
- The fluid properties are constant
- Body force and radiation are negligible.

To ensure that the fluid is hydrodynamically fully developed, we set the entrance length to be longer than the entrance length calculated from a turbulent flow[38], namely:

$$L_{en} = D 4.4 Re^{1/6} \quad (3.1)$$

Taking the largest Reynolds number to be  $Re=85784$  and the hydraulic diameter to be 64 mm, the entrance length of a turbulent flow would be 1866 mm. The entrance length for the present work was set at 1900 mm. Beyond the length of 1866 mm from the inlet, it is assumed that the boundary layer no longer develops with distinct characteristics.

### 3.3 Governing Equation

Prediction of the velocity profile and the pressure involves the continuity, momentum and energy equation.

$$\nabla \cdot \mathbf{u} = 0 \quad (3.2)$$

$$\rho_f (\mathbf{u} \cdot \nabla \mathbf{u}) = -\nabla p + \mu_f \nabla^2 \mathbf{u} \quad (3.3)$$

$$\rho_f c_{pf} \mathbf{u} \cdot \nabla T = k_f \Delta T \quad (3.4)$$

where the  $\mathbf{u}$ ,  $T$ ,  $p$  are the fluid's velocity, temperature, and static pressure respectively.

The fluid properties include the density ( $\rho_f$ ), dynamic viscosity ( $\mu_f$ ), heat capacity ( $c_{pf}$ ), and the thermal conductivity ( $k_f$ ). Two more equations involved for the  $k - \omega$  SST scheme are the turbulent kinetic energy equation and the specific turbulent dissipation rate; both are thoroughly discussed in [39, 40].

### 3.4 Boundary conditions

The boundary conditions for this present work include [8]:

*Inlet:* Reynolds of 27500, 38600, 52600, 63300, 74300, and 86500 ;  $T_{inlet} = 310.5 \text{ K}$

*Heated Plate:*  $\dot{q}'' = 1110 \text{ W/m}^2$

*Outlet:*  $P = 0 \text{ Pa}$ . (gauge pressure)

The definition of the Reynolds number defined in the experimental work of Alfarawi et al. [8] is

$$\text{Re} = \frac{U_m D}{\nu} \quad (3.5)$$

Where  $U_m$  is the mean velocity obtained from the ratio of flow rate ( $Q$ ) to the cross-sectional area of the duct ( $A_c$ ),  $D$  is the hydraulic diameter, and  $\nu$  is the kinematic viscosity.



### 3.5 Solver

ANSYS FLUENT operates under the finite volume, cell-centered treatment of the governing equation. Two options of the numerical solvers to couple the pressure and velocity are available, namely: pressure-based and density-based solvers. Displayed in Table 3.1, the pressure-based P-u coupling is suitable for incompressible flow, while the density-based P-u coupling is compatible with compressible flows.

Table 3. 1 Solver available in ANSYS 18 [40]

Solver based	Description
Pressure-based	Low speed incompressible flow Pressure field provided Coupled model more accurate than segregated model.
Density-based	High speed compressible flow Pressure calculated from equation of state. Includes interphase coupling

The pressure-based solver can be classified mainly into two classes, namely: the segregated algorithm (SIMPLE, SIMPLEC, PISO) and the coupled algorithm. The segregated algorithm does all calculations in steps. That is the fluid properties (e.g. density, viscosity, specific heat) are used to solve the momentum equation, where the velocity field is fed to solve for the pressure correction, followed by the mass flux, energy and turbulence. The cycle repeats until results converge. The Coupled algorithm use the fluid properties to simultaneously solve the velocity and pressure field, followed by the mass flux, energy, turbulence until convergence. In this work, SIMPLE segregated numerical scheme was chosen.

Table 3. 2 Segregated numerical schemes in ANSYS [40]

Solver based:	Description
SIMPLE	A guessed pressure value is used to solve each component of the velocity field, which is used to find the pressure correction. The discretized for other quantities based on $P$ , $u$ , $v$ , $w$ are calculated. Cycle repeats.
SIMPLEC	Same as simple, but the solver accelerates convergence where $P$ - $v$ calculation is the main deterrent
PISO	Repeats calculation for SIMPLE and SIMPLEC, but contains neighbor correction and skewness correction, which is the correction for mass flux at the interface -Large CPU-time

### 3.6 Turbulence Model

Table 3.3 briefly summarizes the turbulence schemes offers by ANSYS. The models employing Boussineq approach are fast and robust. Among these, two commonly used turbulence formulations for heat transfer are  $k - \varepsilon$  and  $k - \omega$ . The  $k - \varepsilon$  turbulence formulation is suitable for predictions of the far freestream. The prediction of the onset of flow separation is computed too late and becomes problematic in giving results which are too optimistic. Meanwhile, the  $k - \omega$  has been adjusted to emphasize the near wall phenomena. The  $k - \omega$  turbulence model is classified into three subclasses, namely: Standard  $k - \omega$ , Baseline (BSL)  $k - \omega$ , and Shear-stress transport (SST)  $k - \omega$  [40]. This section explains the formulation of the  $k - \omega$  turbulent model. Finally, shear -stress transport (SST)  $k - \omega$  turbulence was chosen for the present work.

Table 3. 3 Turbulence model offers in ANSYS 18 [40].

TURBULENCE MODEL	SPECIALTY	FLOW TYPE	CPU-TIME	Re Range	APPLICATIONS
<b>RANS</b>	use for time average of equation of motion				
<b>Filtered-N.S. (LES)</b>	LES: resolves wide range of time and length scales  Low-pass filtering: time-off for short length scale.	Incompressible and Compressible	Slow, Faster than LES alone		
<b>Spalart-Allmaras Model</b>	Boussineq technique relates the Reynolds stress to the velocity gradient is used to approximate $\mu_t$ .	-	Fast	Low	Aerodynamics, Industrial applications
<b><math>k - \varepsilon</math></b>	*Use Boussineq technique to find $\mu_t$ . *Additional equations: -turbulent kinetic energy -turbulent dissipation rate *Accurate Swirling Flow	Incompressible and Compressible	Fast	Low and High	Industrial flow, Heat transfer simulation
<b><math>k - \omega</math></b>	*Use Boussineq technique to find $\mu_t$ . *Additional equations: -turbulent kinetic energy -specified dissipation rate Near-wall calculation *SST: accurate onset of flow separation from smooth surface *Provide damping for VOP and Mixture models. *Include roughness correlations	Incompressible and Compressible	Fast		Adverse pressure gradient, Airfoil, Transonic shock wave

$K - \omega$  Turbulence involves two more additional equations to the governing equations of the same form, the turbulence kinetic energy equation (Eq. 3.4) and the specific dissipation rate equation (Eq. 3.5) .

Turbulence kinetic ( $k$ ) equation:

$$\frac{\partial(\rho k)}{\partial t} + \frac{\partial(\rho k u_i)}{\partial x_i} = \frac{\partial}{\partial x_j} \left( \Gamma_k \frac{\partial k}{\partial x_j} \right) + G_k - Y_k + S_k \quad (3.4)$$

Specific dissipation rate ( $\omega$ ) equation:

$$\frac{\partial(\rho \omega)}{\partial t} + \frac{\partial(\rho \omega u_i)}{\partial x_i} = \frac{\partial}{\partial x_j} \left( \Gamma_\omega \frac{\partial \omega}{\partial x_j} \right) + G_\omega - Y_\omega + S_\omega \quad (3.5)$$

where the  $k$  and  $\omega$  are the turbulence kinetic energy and the specific dissipation rate. In the diffusion terms,  $\Gamma_k$  and  $\Gamma_\omega$  are the effective diffusivity of  $k$  and of  $\omega$ , respectively. For both equations, last three terms are the generation terms, the dissipation terms, and the source terms. That is,  $G_k$  and  $G_\omega$  are the generation of turbulence kinetic energy and specific dissipation rate. The  $Y_k$  and  $Y_\omega$  are the dissipation of kinetic energy and specific dissipation rate. The  $S_k$  and  $S_\omega$  are the source terms for user defined purposes.

The differences between the Standard, BSL, and SST  $k - \omega$  turbulence schemes differs in the effective diffusivity terms, the generation of  $k$  and  $\omega$ , and their dissipation terms. The BSL develops from the Standard model. Likewise, the SST adjusted the BSL formulation.

The effective diffusivities  $\Gamma_k$  and  $\Gamma_\omega$  are define as follows:

$$\Gamma_k = \mu + \mu_t / \sigma_k \quad (3.5)$$

$$\Gamma_\omega = \mu + \mu_t / \sigma_\omega \quad (3.6)$$

Where  $\mu$ ,  $\mu_t$ ,  $\sigma_k$ ,  $\sigma_\omega$  are the dynamic viscosity, the turbulent viscosity, and the turbulent Prandtl numbers for  $k$  and  $\omega$ . Table 3.4 explains the forms of turbulence viscosity for different  $k - \omega$  formulations. Table 3.5 displays the turbulent Prandtl numbers for both  $k$  and  $\omega$  for the different  $k - \omega$  formulations.

The generation of the kinetic energy is non-linear

$$G_k = -\rho \overline{u'_i u'_j} \frac{\partial u_j}{\partial x_i} \quad (3.7)$$

This Boussinesq hypothesis allows this to be simplified as

$$G_k = \mu_t S^2 \quad (3.8)$$

Where  $S$  is the modulus of the mean rate-of-strain tensor defined in the same way as the  $k - \varepsilon$  model. This term is the same for all the three formulations of  $k - \omega$  .

Meanwhile, the generation of  $\omega$  is specified in Table 3.6. The dissipation of  $k$  and  $\omega$  are specified in Table 3.7 and 3.8, respectively.

Table 3.4 The turbulence viscosity for different  $k - \omega$  formulations [40].

	Standard $k - \omega$	Baseline $k - \omega$	SST $k - \omega$
$\mu_t$	$\mu_t = \alpha^* \frac{\rho k}{\omega},$		$\mu_t = \frac{\rho k}{\omega} \frac{1}{\max[\frac{1}{\alpha^* a_1 \omega}, \frac{S F_2}{a_1 \omega}]},$
	For Low Re: $\alpha^* = \alpha_\infty^* \frac{\alpha_\infty^* + Re_t/R_k}{1 + Re_t/R_k},$ Where $Re_t = \frac{\rho k}{\mu \omega}, R_k = 6, \alpha_\infty^* = \frac{\beta_i}{S}, \beta_i = 0.072$  For High Re: $\alpha^* = \alpha_\infty^* = 1$		Where $F_2 = \tanh(\phi_2^2),$ $\phi_2 = \max[2 \frac{\sqrt{k}}{0.09 \omega y}, \frac{500 \mu}{\rho y^2 \omega}]$

where  $y$  is the distance to the next surface.

Table 3.5 Turbulence Prandtl number for  $k$  and  $\omega$  [40].

	Standard $k - \omega$	Baseline $k - \omega$	SST $k - \omega$
$\sigma_k$	2.0	$\sigma_k = \frac{1}{F_1/\sigma_{k,1} + (1 - F_1)/\sigma_{k,2}}$	
$\sigma_\omega$	2.0	$\sigma_\omega = \frac{1}{F_1/\sigma_{\omega,1} + (1 - F_1)/\sigma_{\omega,2}}$	
		Where $F_1 = \tanh(\phi_1^4)$ $\phi_1 = \min[\max[\frac{\sqrt{k}}{0.09 \omega y}, \frac{500 \mu}{\rho y^2 \omega}], \frac{4 \rho k}{\sigma_{\omega,2} D_\omega^+ y^2}]$ $D_\omega^+ = \max[2 \rho \frac{1}{\sigma_{\omega,2}} \frac{\partial k}{\partial x_j} \frac{\partial \omega}{\partial x_j}, 10^{-10}]$  Where $\sigma_{k,1} = 1.176, \sigma_{k,2} = 1.0, \sigma_{\omega,1} = 2.0, \sigma_{\omega,2} = 1.168$	

where is the positive portion of the cross-diffusion term.

Table 3.6 The generation of specific dissipation rate  $\omega$  [40].

	Standard $k - \omega$	Baseline $k - \omega$	SST $k - \omega$
$G_\omega$	$G_\omega = \alpha \frac{\omega}{k} G_k$	$G_\omega = \alpha \frac{\alpha^*}{v_t} G_k$	
	For Low Re: $\alpha = \frac{\alpha_\infty}{\alpha^*} \left( \frac{\alpha_0 + Re_t/R_\omega}{1 + Re_t/R_\omega} \right)$ For High Re: $\alpha = \alpha_\infty = 1$		
	Where $\alpha_\infty = 0.52, \alpha_0 = 1/9, R_\omega = 2.95$	Where $\alpha_\infty = F_1 \alpha_{\infty,1} + (1 - F_1) \alpha_{\infty,2}$ , Where $\alpha_{\infty,2} = \frac{\beta_{i,2}}{\beta_\infty^*} - \frac{k^2}{\sigma_{\omega,2} \sqrt{\beta_\infty^*}}$	

Table 3.7 The dissipation of turbulence kinetic energy,  $k$  [40].

	Standard $k - \omega$	Baseline $k - \omega$	SST $k - \omega$
$Y_k$	$Y_k = \rho \beta^* f_\beta k_\omega$		
	$f_\beta = \begin{cases} 1, & x_k \leq 0 \\ \frac{1 + 680x_k^2}{1 + 400x_k^2}, & x_k > 0 \end{cases}$ $\beta^* = \beta_i^* [1 + \zeta^* F(M_t)]$ $\beta_i^* = \beta_\infty^* \left( \frac{\frac{4}{15} + (R_t/R_\beta)^4}{1 + (R_t/R_\beta)^4} \right)$ $\zeta^* = 1.5, R_\beta = 8, \beta_\infty^* = 0.09$		

Table 3. 8 The dissipation of specific dissipation rate  $\omega$  [40].

	Standard $k - \omega$	Baseline $k - \omega$	SST $k - \omega$
$Y_\omega$	Where  and	$Y_\omega = \rho \beta f_\beta \omega^2$ $f_\beta = \frac{1+70x_\omega}{1+80x_\omega},$ $x_\omega = \frac{\Omega_j \Omega_{jk} S_{ki}}{(\beta_\infty^* \omega)^3},$ $\Omega_{ij} = \frac{1}{2} \left( \frac{\partial u_i}{\partial x_j} - \frac{\partial u_j}{\partial x_i} \right)$	
	$\beta = \beta_i \left[ 1 - \frac{\beta_i^*}{\beta_i} \zeta^* F(M_t) \right]$	Where	$\beta_i = F_1 \beta_{i,1} + (1 - F_1) \beta_{i,2}$
	For High Re: $\beta_i^* = \beta_\infty^* = 0.09$ Incompressible: $\beta_i = 0.072$ Compressible: $F(M_t) = \begin{cases} 0 & M_t \leq M_{t,0} \\ M_t^2 - M_{t,0}^2 & M_t > M_{t,0} \end{cases}$ $\zeta^* = 1.5, M_t^2 = 2k/a^2,$ $M_{t,0} = 0.25, a = \sqrt{\gamma RT}$	Where	$\beta_{i,1} = 0.075,$ $\beta_{i,2} = 0.0828$

Where  $S_{ij}$  is the strain rate.

Table 3. 9 Spatial discretization offers in ANSYS 18 [40].

Solver based	Description
First order upwind	A quantity is specified to the centre of the cell
Power-law Scheme	Use the exact solution to interpolate quantity values for the cell face
Second-order upwind	Multidimensional linear construction of the quantity value at the cell face
First-to-higher order blending	–
Central differencing	Calculate the face value from the central value of cells that share the face -For improved accuracy for LES turbulence model -Can lead to unphysical oscillation
Bounded central differencing	Combine central differencing and 2 <sup>nd</sup> order upwind Improved unphysical oscillations
QUICK	-Is a weighted average of 2 <sup>nd</sup> order-upwind and central interpolation -for quadrilateral and hexahedral mesh

## CHAPTER 4 RESULTS AND DISCUSSION

### 4.1 Numerical validation with experiments

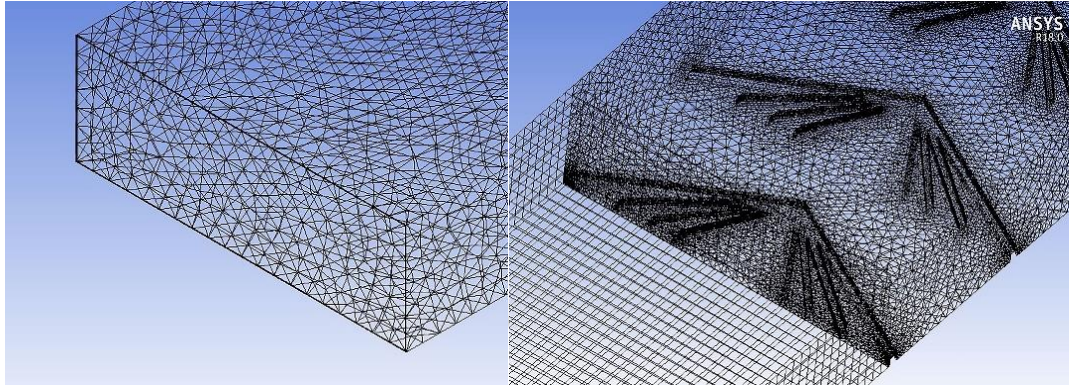
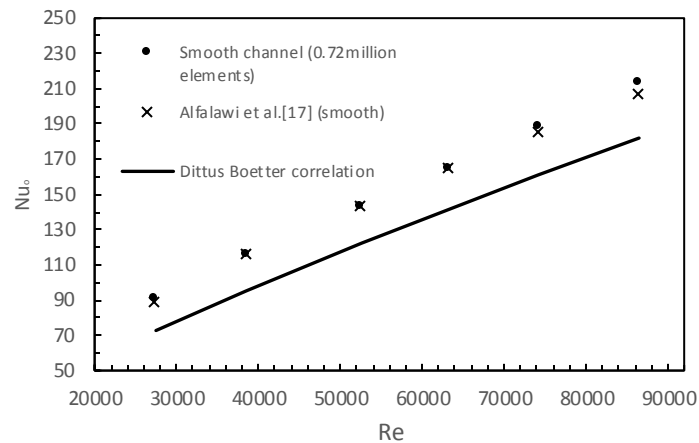


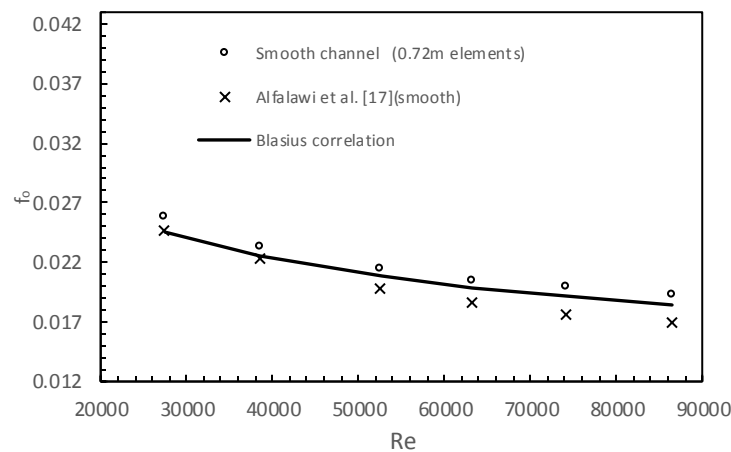
Figure 4. 1 Mesh of smooth channel

Figure 4. 2 Mesh of channel with ribs

Grid independency test had been performed for the smooth channel using the cell numbers of 0.72M, 1.1M, 4.6M and 11.2M in verification with the experiments of Alfarawi et al [8]. At the cell number of 0.72M, the respective variation of the Nusselt number and friction factor were 1.1% and 2.3% from values obtained using 1.1M cells, and grid independency was achieved. In comparison with the experiments of Alfarawi et al. [8], Figure 5.1 (a) shows that the Nusselt number of the simulation differed by 0.1%-3.3% and Figure 5.1 (b) shows that the friction factor deviated by 4.3%-14.7%. The number of cells chosen corresponded to the grid size of 6 mm with 5 inflation layers, where the first inflation layer was  $5 \times 10^{-5}$  m.



(a) Nusselt number of the smooth channel,  $Nu_0$  vs.  $Re$



(b) Friction factor of the smooth channel,  $f_0$  vs.  $Re$

Figure 4. 3 Validation with experiment [8] for a smooth channel.

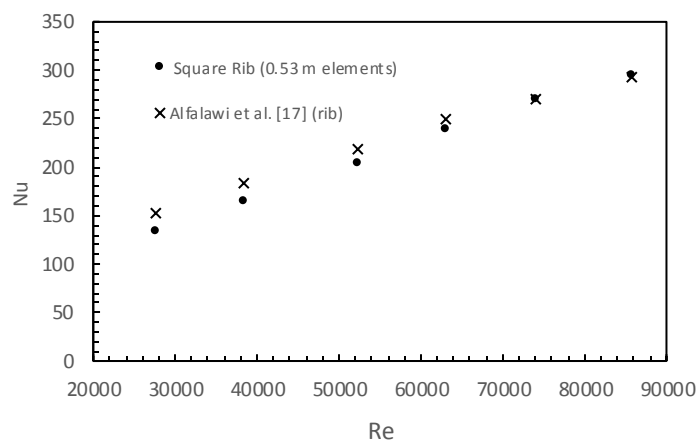
Grid independency test was also performed with the roughened channel with rectangular ribs at the cell numbers of 0.175M, 0.53M, 0.723M, 1.6M and 3.4M. Grid independency was established at 0.53M cells with cell structures shown in Figure 5.2. Numerical simulations tested against experiments of Alfarawi et al. [8] with roughened channel revealed in Figure 5.4 (a) that the Nusselt number variation within 0.3%-12.3%, and Figure 5.4 (b) showed that the deviation of the friction factor was within 3.3-14.0% range. Shown in Figure 5.4 (a) the Nusselt numbers were also compared with Dittus Boetter correlation (Eq. 4.1), as cited in [41]. Shown in Figure



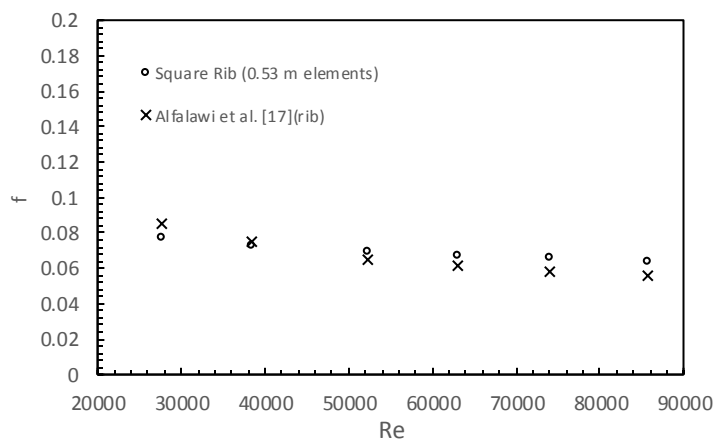
5.4 (b), the friction factors were also validated with Blasius correlation (Eq. 4.2), as cited in [41].

$$\text{Dittus Boetter correlation: } Nu = 0.023Re^{0.8}Pr^{0.4} \quad , \text{ for heating.} \quad (4.1)$$

$$\text{Blasius correlation: } f = 0.316Re^{-0.25} \quad (4.2)$$



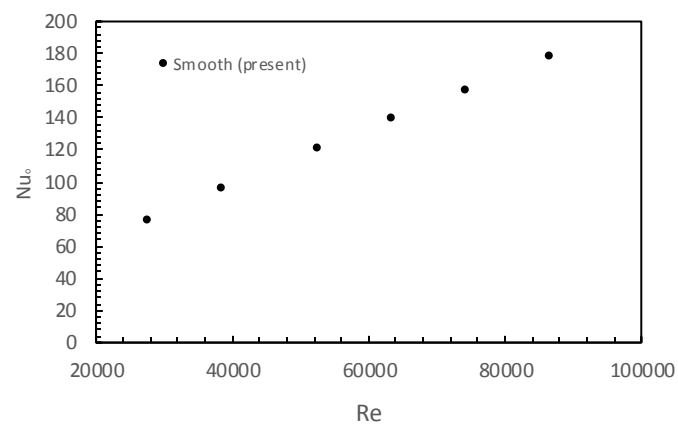
(a) Nusselt number of the roughened channel, Nu vs. Re



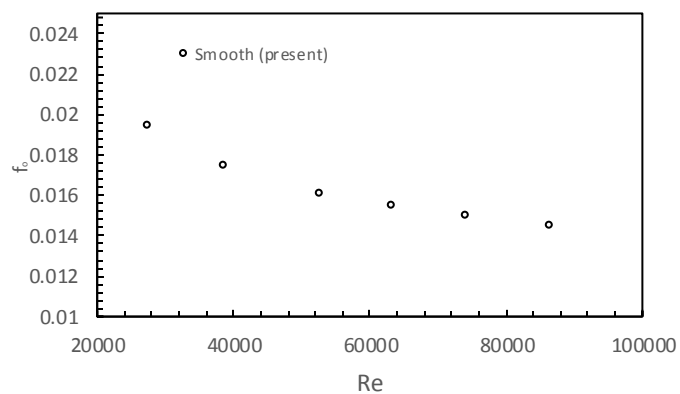
(b) Friction factor of the roughened channel, f vs. Re

Figure 4. 4 Validation with experiment [8] for a channel with ribs.

Since the tested length of both the smooth and roughened channel of this present work were elongated to 100 cm, unlike Alfarawi et al. [8], the Nusselt number and friction factor for the smooth channel for this present work were recomputed and are shown in Figure 4.5.



(a) Nusselt number vs. Re

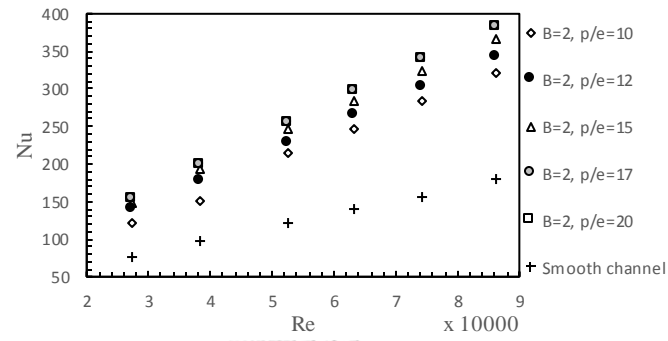


(b) Friction factor vs. Re

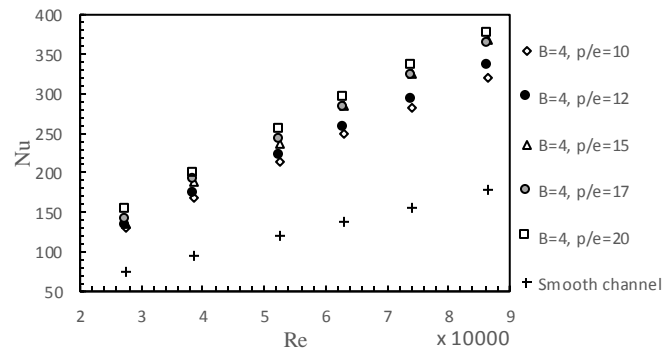
Figure 4.5 Nusselt number and friction factor for the smooth channel for this simulation.

### 4.3 The Thermal Hydraulic Interpretation

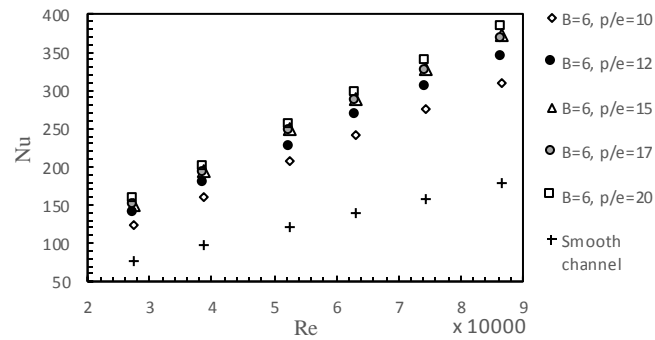
#### 4.3.1 Effects of the Reynolds number



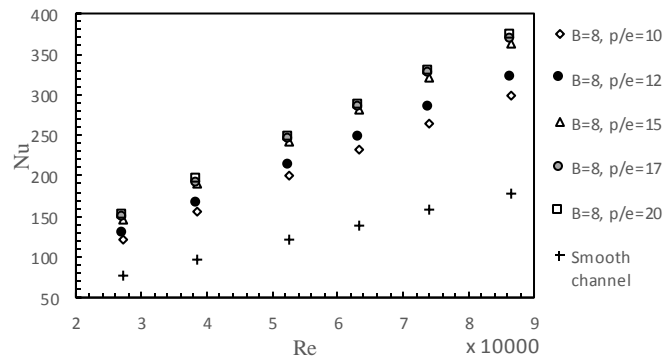
(a) V-down,  $B=2$



(b) V-down,  $B=4$



(c) V-down,  $B=6$



(d) V-down,  $B=8$

Figure 4. 6 Nu vs. Re

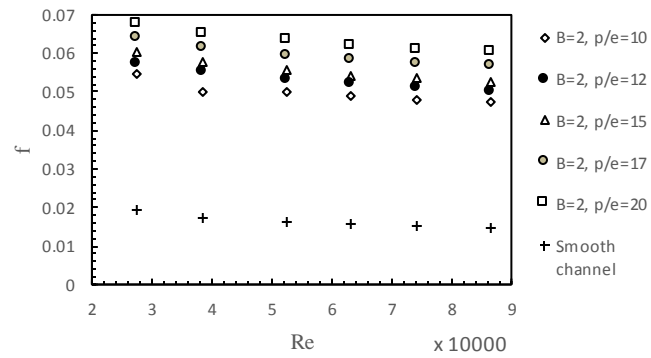
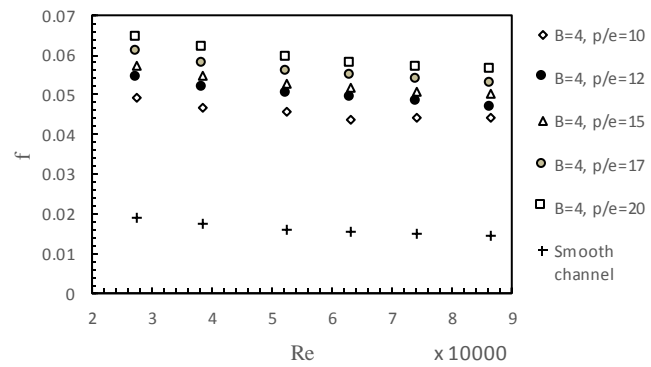
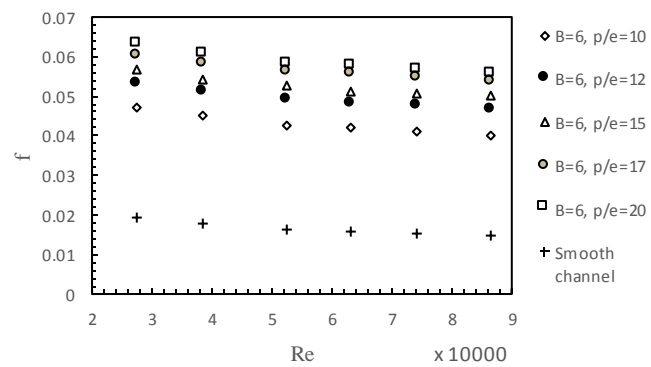
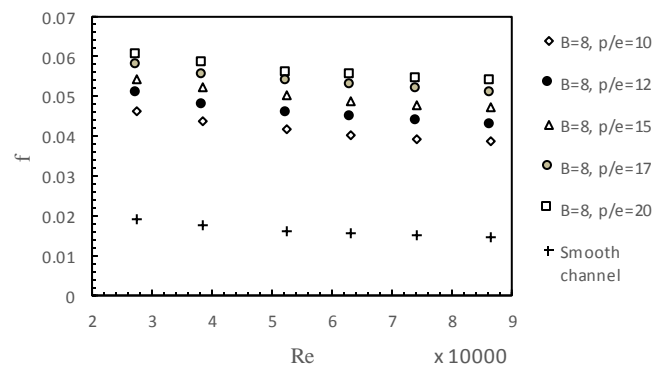
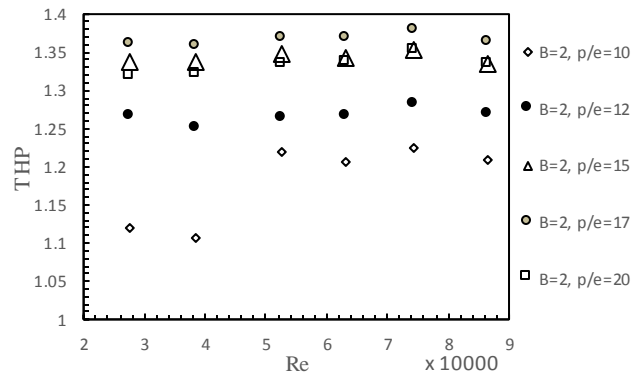
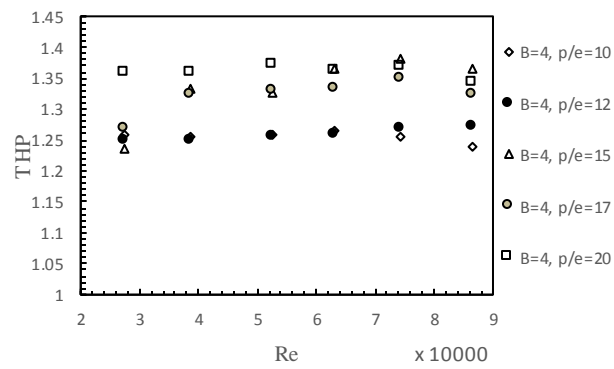
(a) V-down,  $B=2$ (b) V-down,  $B=4$ (c) V-down,  $B=6$ (d) V-down,  $B=8$ Figure 4. 7  $f$  vs.  $Re$

Figure 4.6-4.7 show the relationship between the Reynolds number with the Nusselt number, friction factor and the hydraulic performance at various pitch ratio for the four rib types. From Figure 4.6 and Figure 4.7, as the Reynolds number increases, the Nusselt number increases while the friction factor decreases as expected, for all channels roughened and smooth. In particular, both the Nusselt number and friction factor of the roughened channel surpass that of the smooth channel. The increased of the Nusselt number with increasing Reynolds number is due to the thinning of the laminar sub-layer in the process of flow separation formation [23] and the increase in the vorticity strength of the secondary flow along the V-rib with higher flow velocity [42]. The increase in the Reynolds number also shorten the distance of the reattachment point from the upstream rib [42]. Thereby, convection heat transfer improves.

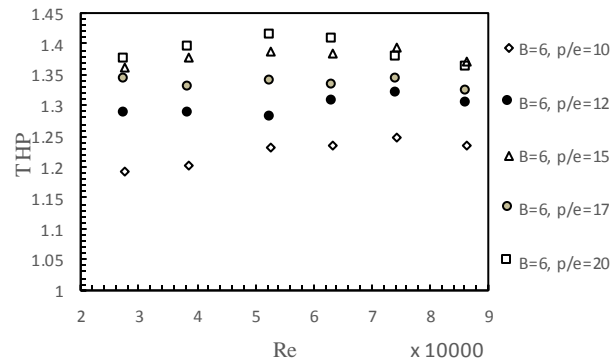
The thermal hydraulic performance (THP) or the thermal performance enhancement factor (TEF) is defined in Eq. 2.11 of Section 2.3. The relationship between the thermal hydraulic performance and the Reynolds number is specific to rib types. Since the Nusselt number increases with the Reynolds number while the friction factor decreases, it is expected that the THP would increase with increasing Reynolds number. It would imply that the heat transfer effects rise and outweighs frictional loss that decreases with high flow rate. However, this is only observed for  $B=2$  and  $P/e=10$ , Figure 4.8 (a). On the other hand, for the same branching number and higher pitch ratio, THP appears constant as the Reynolds number increases. What this suggests is that the relative pitch ratio effects should lifts the friction factor as the Reynolds number increase. (This is the trend expected and to be discussed in the following section.) This implies that, high pitch ratio does increase the overall thermal hydraulic performance of the system, but the effects of the flow rate become trivial. For other branching number of  $B=4$ , shown in Figure 4.7 (b), the constancy of THP with Reynolds number is clear. For  $B=6$  and 8, shown in Figure 4.7 (c) and (d), there is a rising followings be a decreasing trend of THP with Reynolds number. The connotation of this is, although the rise in the flow rate improves heat transfer, at some flow speed, friction begins to produce observable negative feedback on the overall heat transfer performance and lower the THP value.



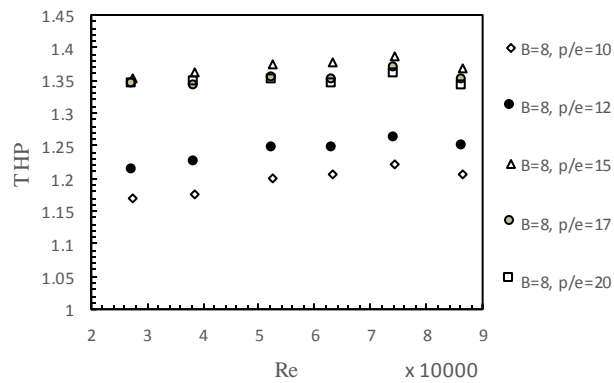
(a) V-down,  $B=2$



(b) V-down,  $B=4$



(c) V-down,  $B=6$



(d) V-down,  $B=8$

Figure 4. 8 Thermal hydraulic performance vs. Re

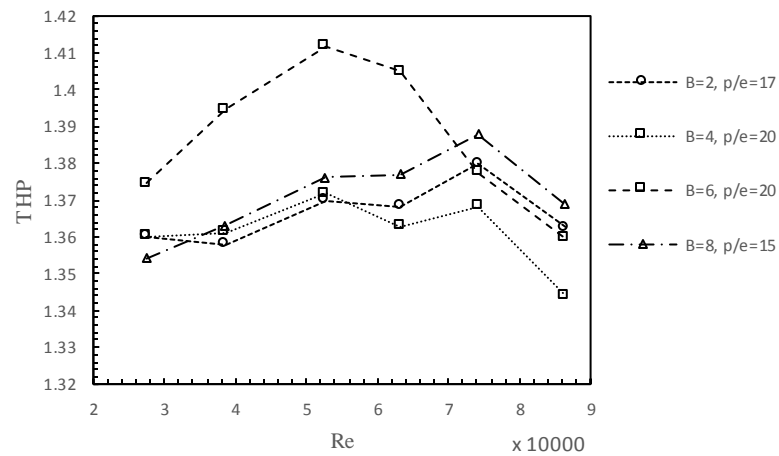
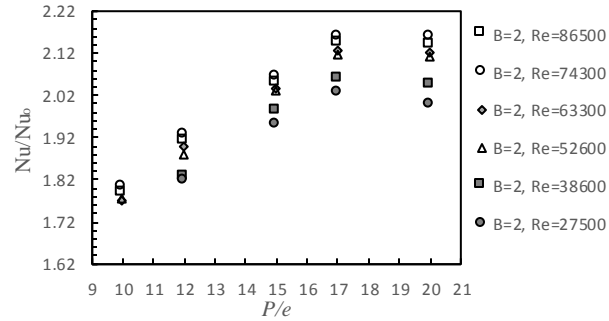
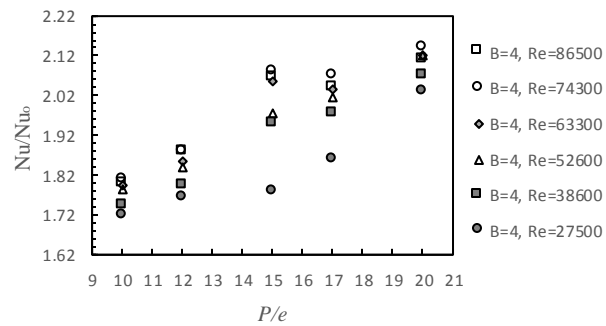
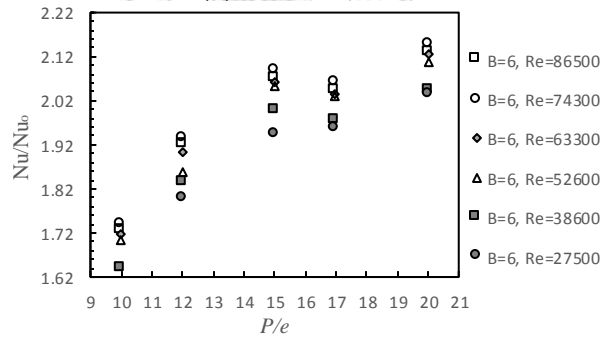
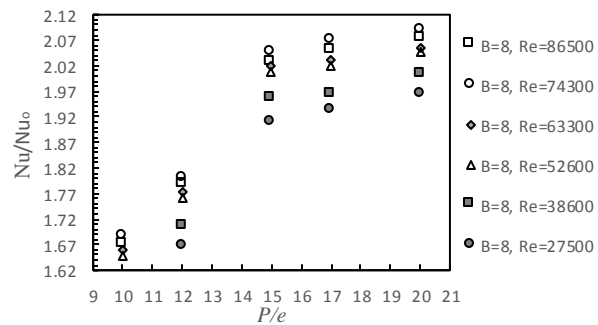


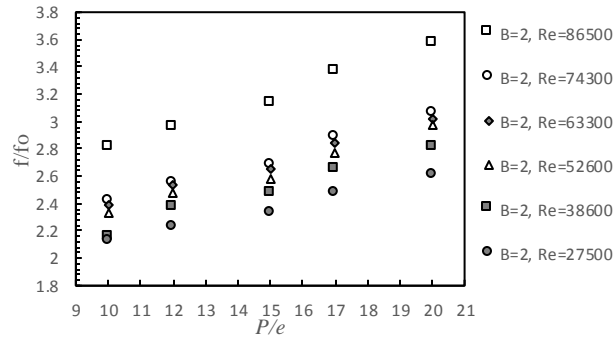
Figure 4.9 THP vs. Re at various the optimal  $P/e$  for specific  $B$ .

Figure 4.9 selects the optimal pitch ratio for each branching number from Figure 4.17. It can be seen that high frictional effects occurs at the Reynolds number greater than around 50000 for  $B=6$ . For other branching number of  $B=2$ , 4, and 8, high frictional effect strikes at the Reynolds number greater than 74000. It can be seen that the optimal pitch ratio is rib-specific. This will be discussed in the following section.

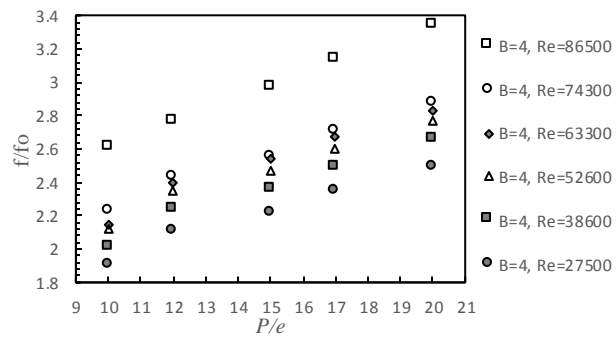
### 4.3.2 Effects of pitch ratio

(a) V-down,  $B=2$ (b) V-down,  $B=4$ (c) V-down,  $B=6$ (d) V-down,  $B=8$ Figure 4. 10  $Nu/Nu_0$  vs.  $P/e$

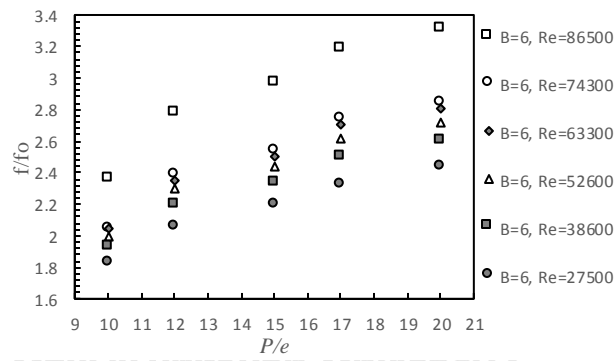




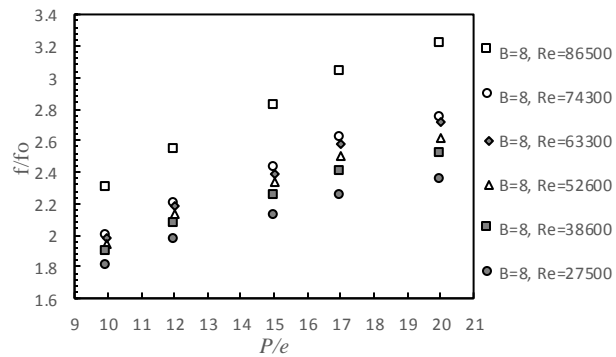
(a) V-down,  $B=2$



(b) V-down,  $B=4$



(c) V-down,  $B=6$



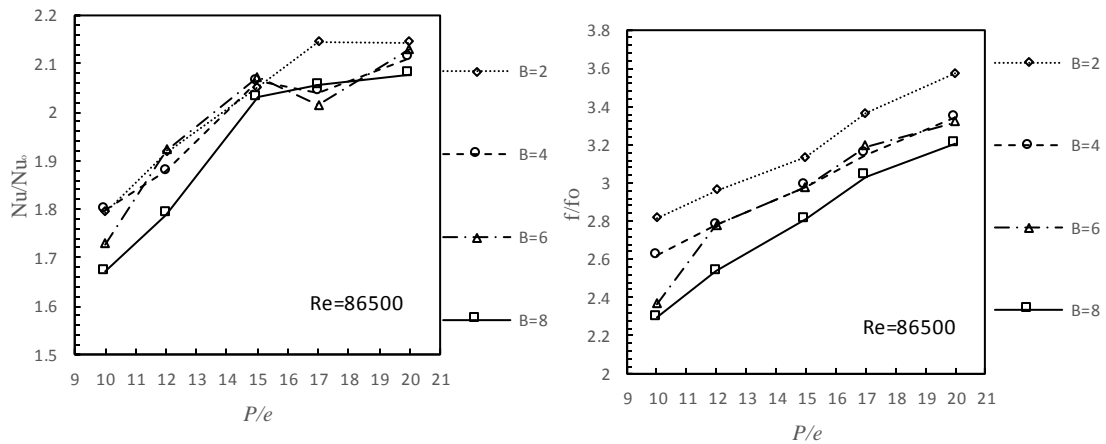
(d) V-down,  $B=8$

Figure 4. 11  $f/f_0$  vs.  $P/e$

The relationship between the Nusselt number ratio and the relative pitch ratio can either be quadratic [16] or quartic [42]. For the four rib cases, Figure 4.10 (a)-(d) show increasing trend of the Nusselt number ratio with the relative pitch ratio which plateau out at a specific relative pitch ratio. The peak Nusselt number ratio is at 20 for all cases. Not shown in the graphs, when the relative pitch ratio is 21, the Nusselt number ratios for all rib cases reduce. From Figure 4.12 (a), an increase in the Nusselt number ratio at pitch ratio of 10 to 20 for  $B=2$  is 1.2 times. The maximum increase in the Nusselt number ratio with pitch from  $P/e$  of 10 to 20 belongs to  $B=6$ , that is 1.49 times. It can be explained that at very low pitch ratio, local reattachment does not occur after every rib. When the pitch ratios increases, the number of reattachment points are adjusted to increase. Thus, behind these ribs thorough mixing and exchange of momentum and heat are achieved due to strong turbulent motion induced by the ribs. The optimal relative ratio corresponds to the relative pitch ratio that allows maximum reattachment points.

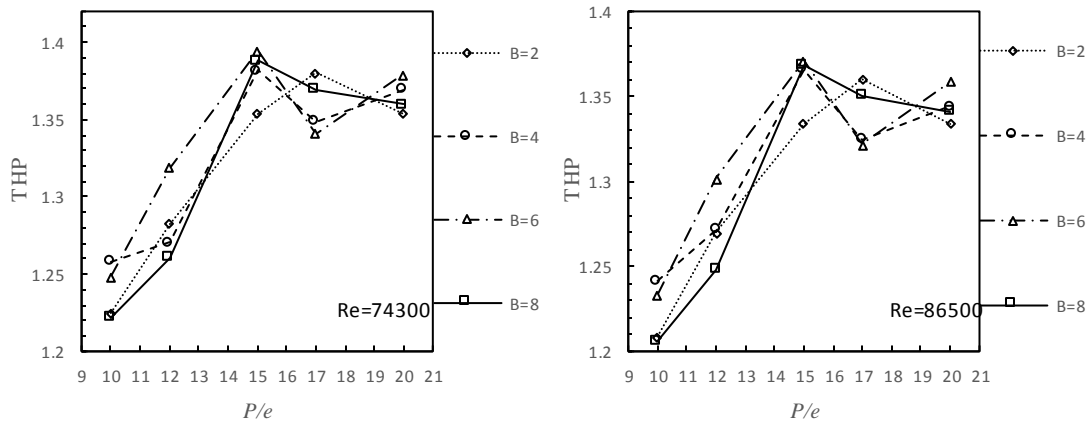
From Figure 4.11, the friction factor ratio increases linearly with the relative pitch ratio. The increase in turbulent motion and near wall collision via increasing the local reattachment points led to an accumulative increase in friction with increasing relative pitch ratios. For the conventional V-rib with  $B=2$ , varying  $P/e$  from 10 to 20 raise the friction factor by 1.27 times. Other branching number of  $B=4$ , 6, and 8 results in an increase of 1.27, 1.4 and 1.4 times increase in the friction factor ratio as the relative pitch ratio increase from 10 to 20.

One noteworthy observation from Figure 4.10-4.11 is that the peak of the friction factor ratio with increasing pitch ratio is at the highest Reynolds number of 86500; however, the peak of the Nusselt number ratio with the relative pitch ratio belongs to the Reynolds number of 74300. It can be viewed that the increased pitch ratio can both increase the heat transfer and friction of the channel, and too high Reynolds number can also lower the heat transfer performance slightly.



(a)  $Nu/Nu_0$  vs.  $P/e$

(b)  $f/f_0$  vs.  $P/e$



(c) THP vs.  $P/e$  at  $Re=74300$

(d) THP vs.  $P/e$  at  $Re=86500$

Figure 4.12 Effects of the relative pitch ratio on heat transfer and pressure drop at different  $B$ .

The combined results of Figure 4.12 (a) and (b) is shown in Figure 4.12 (c)-(d) via the THP formula. From Figure 4.12 (a), the branching number of  $B=2$  to 6 all has higher heat transfer performance than  $B=8$ . The trend of variation with the relative pitch ratio is increasing and coming to a peak at  $P/e=20$ . Correspondingly, in Figure 4.12 (b),  $B=2$  to 6 also has higher friction factor ratio than  $B=8$ . The trend of variation with the relative pitch ratio is a linear rise. Figure 4.12 (c) and (d) show the relationship between the THP and the relative pitch ratio. The THP increases with the relative pitch ratio and peaks at the relative pitch ratio of 15 for both the Reynolds number of 74300 and 86500. At the relative pitch ratio of 15 and  $Re=74300$ , the THP

for  $B=2, 4, 6,$  and  $8$  are  $1.35, 1.38, 1.39$  and  $1.39$  in that order. However, from Figure 4.12 (c) and (d), it can be seen that as the discrepancy between the pitch ratio of 15 to 20 are not so high for all rib cases, the relative pitch ratio between 15 to 20 are all acceptable relative pitch ratios.

### 4.3.3 Effects of the branching number

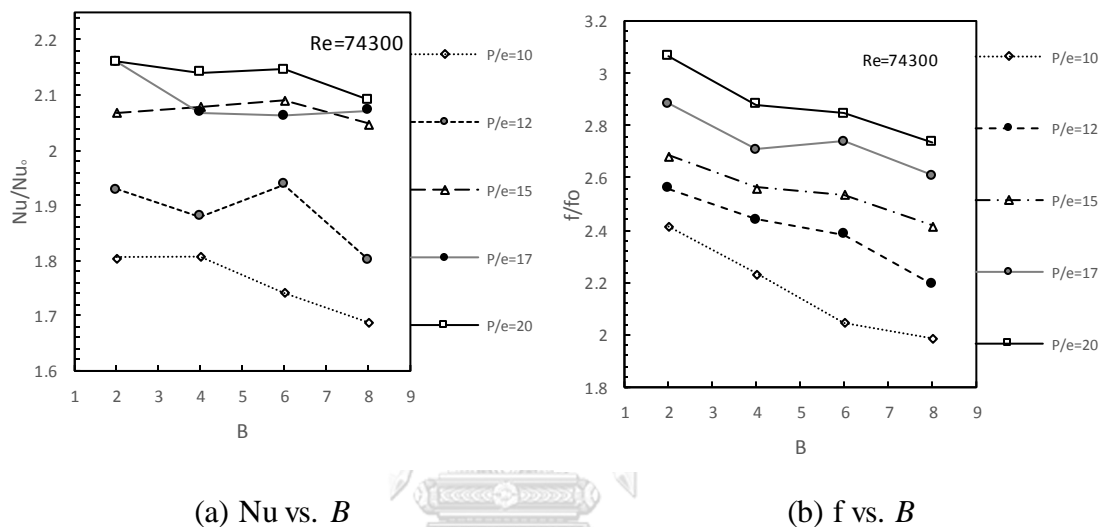


Figure 4.13 Effects of the branching number on heat transfer and frictional loss

Figure 4.13 displays the effect of the branching number on the heat transfer and frictional loss. Recall earlier that low pitch ratio (e.g.  $P/e=10$  or  $12$ ) is where the impingements are skipped for various ribs. In such an arrangement, applying V-ribs with high branching number (e.g.  $B=8$ ), the additional branches close to the channel spanwise symmetrical line will strengthen the particle touching the branch's tips to shoot up and not impinge. Lowering this number, gives rise to higher impingement effects. Therefore, for  $P/e=10$  and  $12$ , higher heat transfer and higher frictional loss is observed for low number of branches (e.g.  $B=2$  or  $4$ ). The trend of the Nusselt number and friction factor are decreasing with increasing branching number.

As the pitch ratio increases (e.g. to  $P/e \geq 15$ ), Figure 4.13 (a) shows that the magnitude of the slopes of  $Nu$  vs.  $B$  decrease. This suggests that the increased number of branches are cooperative towards heat transfer augmentation as opposed to impeding it. Somehow the increased in number of branches should improve the turbulence intensity within the channel. To compare the heat transfer effects due to the branches at high pitch ratio ( $P/e \geq 15$ ), varying the branching number plays no role in improving the Nusselt number.

On the other hand, for high pitch ratio ( $P/e \geq 15$ ), the relationship between the friction factor and the branching number is still decreasing. It can be suggested that this partakes the both the impact of the surface area of collision at the branches' tips verses at the span as well as the increased streamwise travel distance across rib with increasing branching number. On the first account, low branching number (e.g.  $B=2$ ) implies that the immediate initial impact of collision of the stream and rib is on the rib's entire span. Meanwhile, for higher branching number (e.g.  $B=8$ ), the initial impact of collision is first and foremost on the tips of the (eight) branches. It can be presupposed that this reduced surface area of initial collision, subsides frictional loss as fluid traverses the channel. For the second account, when the branching number is low (e.g.  $B=2$ ), the fluid only needs to travel the distance across the square-shaped arc of one branch. However, for high branching number (e.g.  $B=8$ ), the distance the fluid needs to travel from one reattachment point to the next is the length of rib's chord, presuming that reattachment occurs between adjacent ribs. In implication, reattachment effects are either subsided or delayed or reduced with increasing branching number of V-ribs.

The number of branches, although did not seem to significantly improve the heat transfer in the Nusselt number measurement; however, it significantly reduces the pressure drop of the system. At the pitch ratio of 10, increasing the branching number from 2 to 8 lowers the frictional loss by 23%. At the pitch ratio of 20, this reduction would be 12%.

With regards to the pitch ratios, if only the effect of heat transfer is considered to be the overall performance of a roughened channel, then Figure 4.13 (a) shows that the relative pitch of 20 would be optimal. However, in reality friction is taken into account and the following graph of Figure 4.14 reveals that the pitch ratio of 20 is no longer optimal, but the pitch ratio of 15 is.

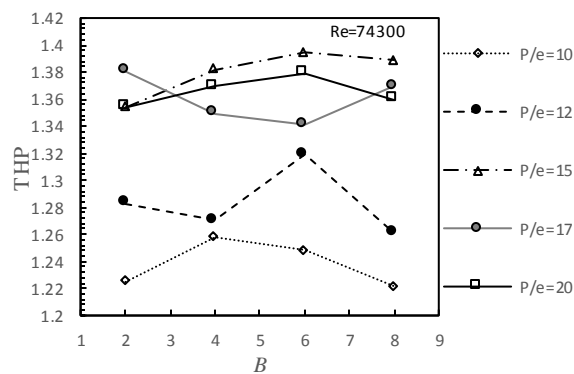


Figure 4. 14 Effects of branching number on thermal hydraulic performance

Figure 4.14 displays the battle of the rib's struggle in improving heat transfer verses the rising friction. For low pitch ratio ( $P/e=10$  and  $12$ ), both  $B=2$  and  $8$  has low overall heat transfer performance. For  $B=2$ , this is because although the heat transfer is very high, the friction produced via reattachments is also very high. For  $B=8$ , the friction effect from reattachments is low, but the heat transfer induced is also very low. This leaves the middle branching number as optimal in the thermal hydraulic performance.

For very high pitch ratio ( $P/e =15$  and  $20$ ), similar trend is observed. The optimal branching number is  $B=6$ . At this branching number, fluids are intensified in its turbulent motion, with frictional loss being subsided from the initial impact of collision and the subsided reattachments.

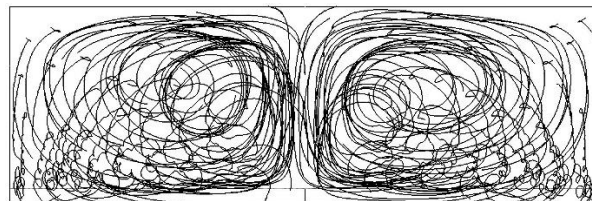
An unusual trend is observed for the relative pitch ratio of  $17$ , where the middle branching numbers (e.g.  $B=4$  and  $6$ ) reveal low THP. It can be observed that at this pitch ratio, there is a reduction on the heat transfer augmentation (see Figure 4.13 (a)), while the frictional loss was not extremely low (see Figure 4.13 (b)).

In various cases, the optimal branching number is 6. If the friction factor is neglected, the optimal pitch ratio for heat transfer augmentation would be 20. Otherwise, the optimal relative pitch ratio that augment the overall thermal hydraulic performance is the pitch ratio of 15. At the relative pitch ratio of 20 and the branching number of 6, the Nusselt number, friction factor and THP compared to the smooth channel are 2.15, 2.85, and 1.38, respectively. At the relative pitch ratio of 15 and the branching number of 6, the Nusselt number, friction factor and THP compared to the smooth channel are 2.08, 2.54, and 1.39, respectively.

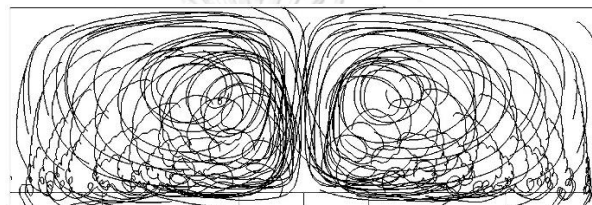


## 4.4 The Physics Insight

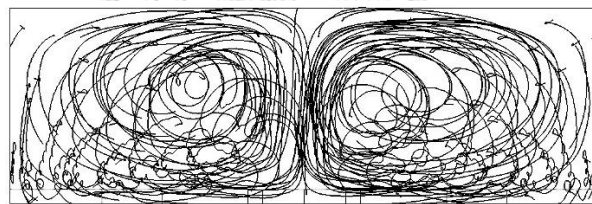
### 4.4.1 Streamline and velocity vector



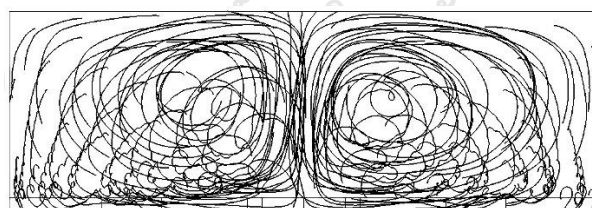
(a) V-rib,  $B=2$



(b) V-rib,  $B=4$



(c) V-rib,  $B=6$



(d) V-rib,  $B=8$

Figure 4. 15 Front View of Streamline



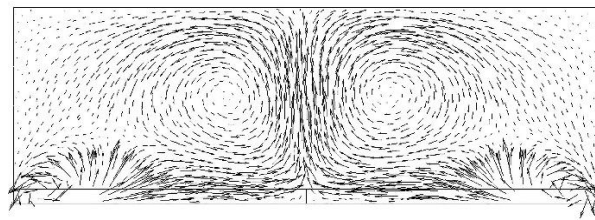
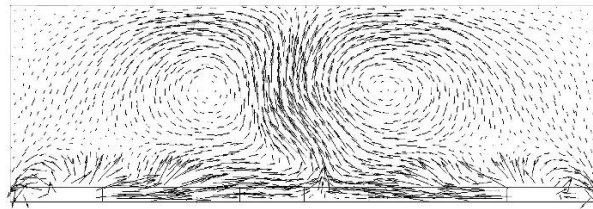
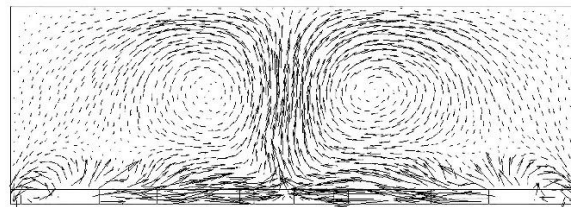
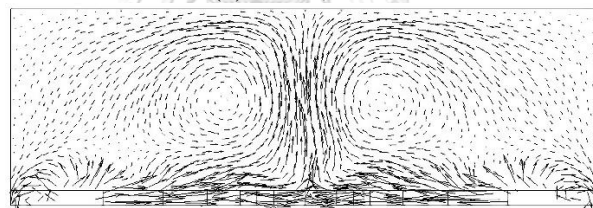
(a) V-rib,  $B=2$ (b) V-rib,  $B=4$ (c) V-rib,  $B=6$ (d) V-rib,  $B=8$ Figure 4.16 Front view of velocity vector ( $x=0.55m$ )

Figure 4.15 display the streamline of fluid traversing the ribs captioned from front view, generated from 100 points. It can be observed fluids touching the tips of the ribs are thrown spiraling centrally for all rib cases.

Meanwhile, Figure 4.16 display the velocity vector of the four rib cases from front view, captioned from a plane sectioning the last rib. It can be seen that rib shape guides the fluid centrally and upwards at the centre. The primary stream forms two cells of secondary flow, rotating co-rotationally. For the V-rib types with the branching number greater than 2, the centrally moving fluids traverse centrally sideways over the branches. In three-dimensional view, the flow structure of Figure 4.15 and Figure 4.16 is the longitudinal secondary flow.

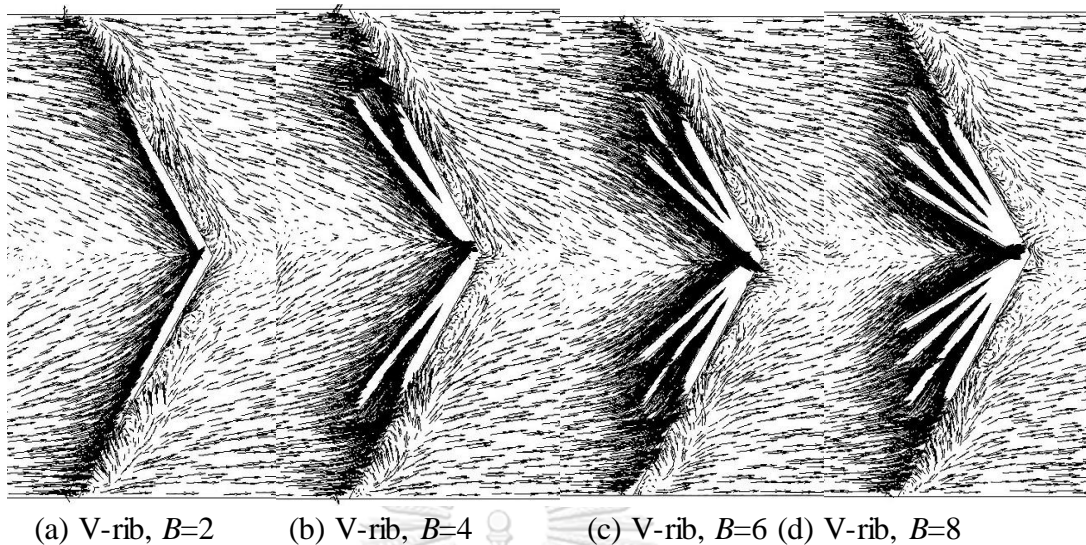


Figure 4.17 Top view of the velocity vector

The top view of the velocity vector is shown in Figure 4.17 for the four rib cases, showing the direction of fluid's motion close to the rib's vicinity. It can be observed that as the fluid approaches the rib's front, fluid made head-on collision with the ribs at the tips for all cases. For the midspan close to the centre of symmetry, fluids more or less glides along the branch at the fore side. Abrupt reattachments occur across the sides of the ribs, close to the side walls, for all cases. The recirculation zone is at the rear mid-span of the rib, prominently behind the apex.

From Figure 4.17, varying the branching number provides two effects. Firstly, the effects of having the branching number increased detains the fluid at the interbranch region. Secondly, as the recirculation zones for  $B=8$  seems wider than those other smaller branching numbers, it appears that lower heat transfer contributes may arise out of the widen recirculation zone with increasing branching number.

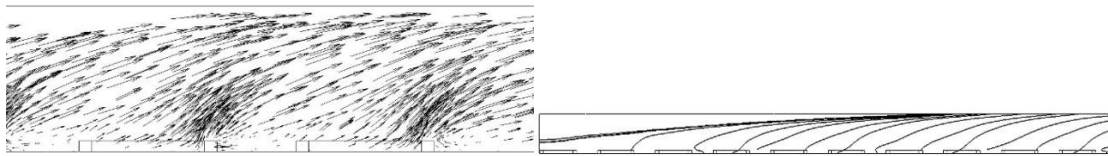
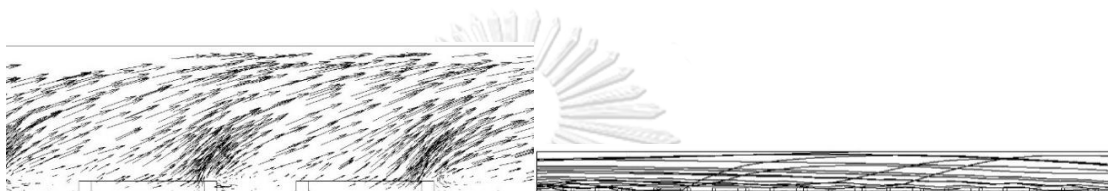
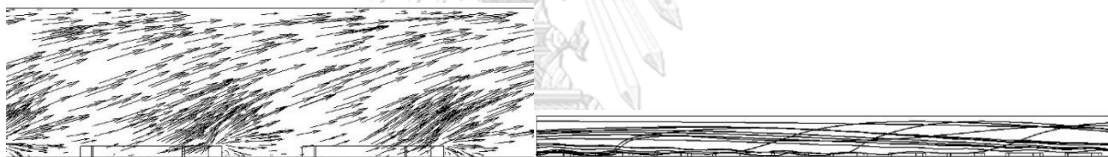
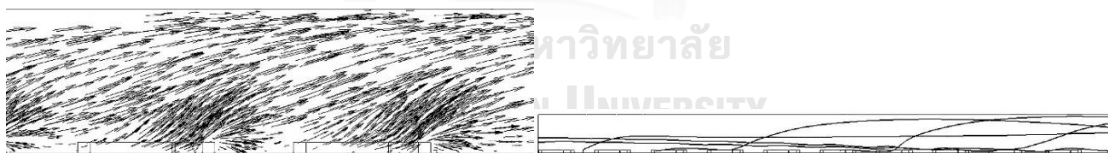
(a) V-rib,  $B=2$ (b) V-rib,  $B=4$ (c) V-rib,  $B=6$ (d) V-rib,  $B=8$ 

Figure 4. 18 Sideview of the velocity vector (left) and sideview of the streamline (right)

(Fluid direction from left to right,  $P/e=20$ )

The velocity vector and the streamline across the ribs in the channel are depicted in Figure 4.18. For high pitch ratios of 20, reattachments occur behind all ribs, where the left figures of Figure 4.18 only display the ninth and the tenth ribs in the channel. The streamlines depicted in Figure 4.18 are taken from plane across the rib's symmetry. Twenty lines of the streamline were set for the displays. For low branching number (e.g.  $B=2$ ), the stream from the apex are always shooting towards the roof. For  $B=4$  and 6, some streams glide along the ribs before being shot upwards. For  $B=4$  and 6, some fluids entering the channel shoots over the first to the tenth ribs and reattach. For  $B=8$ , it can be seen that the fluid velocity close the centre of symmetry of the rib isn't very fast compared to other rib cases. This is perhaps due to the fluid being delayed at the inter-branch space.



### 4.4.2 Vorticity contour

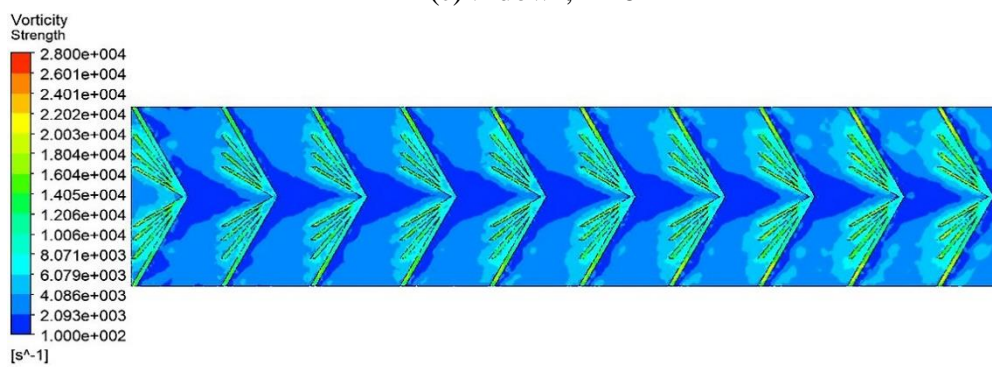
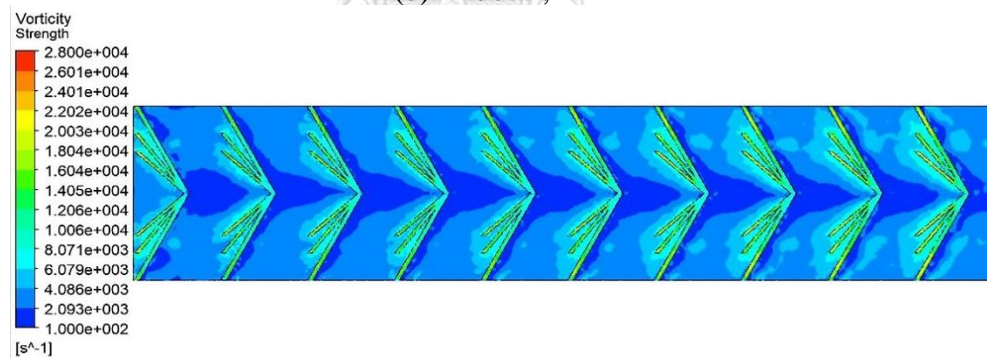
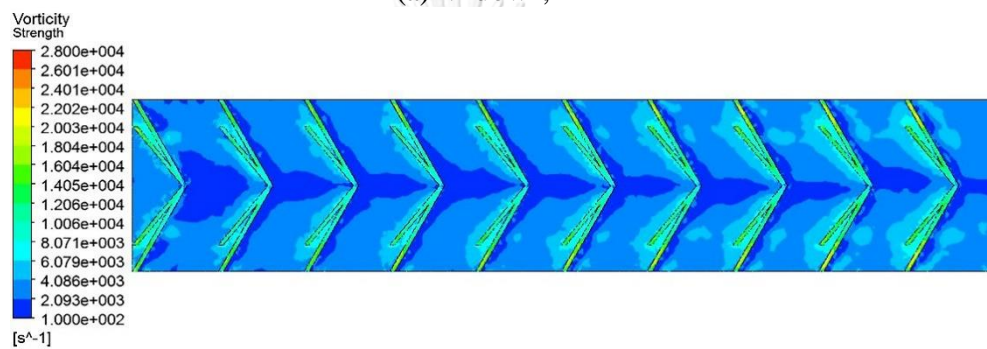
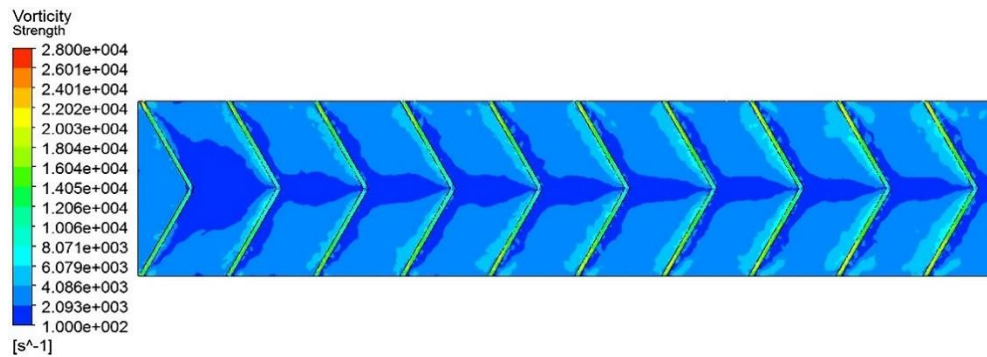


Figure 4. 19 Top view of the vorticity contour for  $P/e=20$  and  $Re=86500$ .

Figure 4.19 shows the vorticity contours from top view. The vorticity strength can be class in zones of high, medium, and low vorticity strength. High vorticity strength belongs to the tip of the branches, the surface on top of the rib, and the inter-rib space that are coloured yellow, green and bright blue. Near wall vorticity in this region is high as the rib induces turbulence there. Medium vorticity strength belongs to the reattachment region that trails from the rear of the tip of the longest branch to the front of the next rib. This is coloured light dull blue in Figure 4.19. As this is a smooth region, circulation is not as high as above the roughness surface. Low vorticity strength is the rear proximity of the rib, behind the apex, extending to the front of the next apex. This is coloured as dark blue.

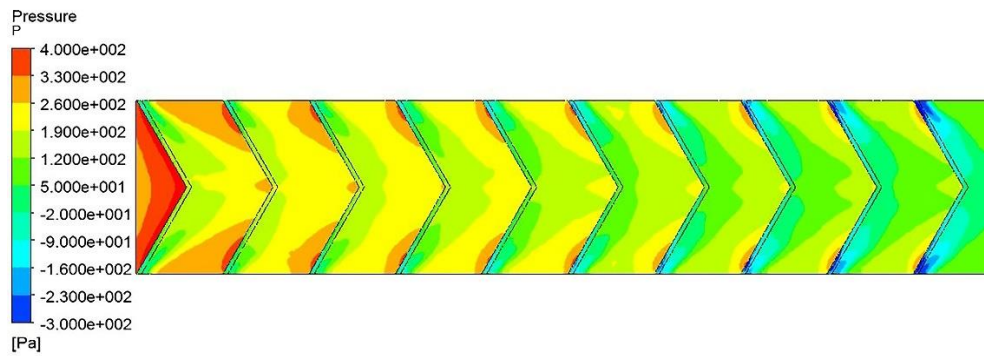
For  $B=2$ , the surface area for higher vorticity strength near wall is small, due to the low surface area of the ribs. The zones of low vorticity strength starts off at the entrance being wide, and gets thinner and thinner along the tested channel length.  $B=2$  is characterized by an overall dominated surface area of medium strength vorticity with impingement effects being high for higher pitch ratio of 20.

For  $B=4$ , the surface area of high vorticity strength expanded due to the increased number of branches. The surface area of low vorticity strength remains low, although slightly larger than  $B=2$ .

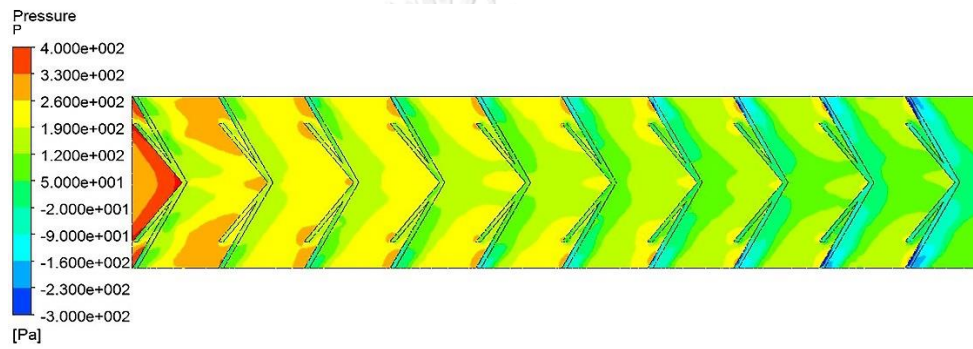
For  $B=6$ , and 8, both the surface area for high and low vorticity strength are enlarged. Particularly for  $B=8$ , the zone of low circulation very much reduce the surface area of the medium strength vorticity. The case for  $B=8$  is where the battle between positive heat transfer effects and negative feed back of the pressure drop can significantly gives an overall slightly reduced thermal hydraulic performance.



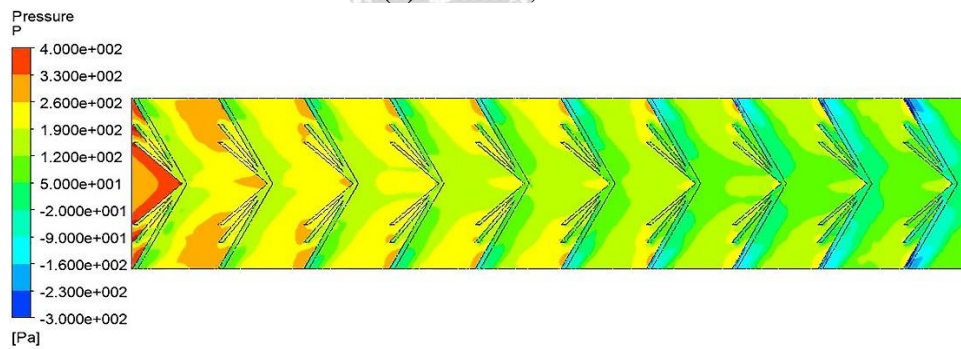
### 4.4.3 Pressure contours



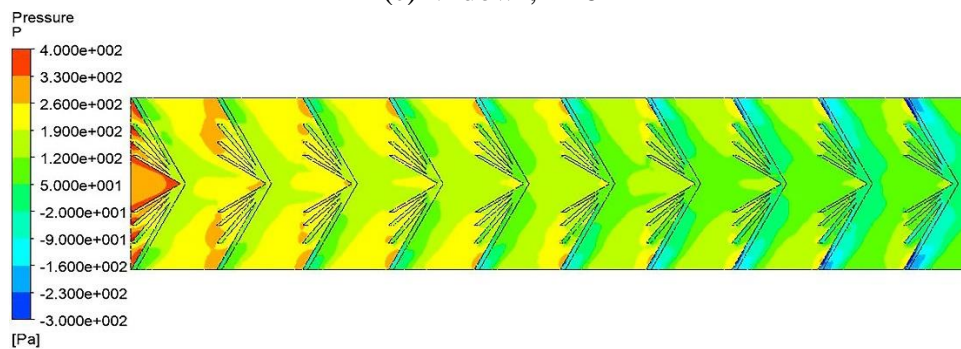
(a) V-down,  $B=2$



(b) V-down,  $B=4$



(c) V-down,  $B=6$



(d) V-down,  $B=8$

Figure 4. 20 Pressure contour for  $P/e=20$  and  $Re=86500$ .

Figure 4.20 shows the pressure contour maps for different V-rib shapes arranged with  $P/e=20$  and  $Re=86500$ . For  $B=2$ , high pressure impact occupies the entire rib forespan. For subsequent ribs, high pressure of collision, coloured red and orange, remains only close to the leading ends of the ribs. Midspan, foreside of the ribs process medium pressure contributes. While the pressure for the entire rear span of the rib is low. These strength decays long the channel length. For the first few ribs, high impact of collision are experienced at the leading ends of the ribs. For the last few ribs, however, the impact of collusion is shifted to the center of the ribs. This is evident in the local minimum observed at the leading ends of the last few ribs. Similar trends are observed for other banching numbers.

Increasing the branching number of V-ribs subsides the strength of collision for all ribs at the leading ends of the ribs. The accumulative effects of weaken pressure of collision for each rib with high branching number leads to a lower pressure difference across the inlet and outlet of the tested channel compared to channel with lower branching number for V-ribs.



#### 4.4.4 Nusselt number contours

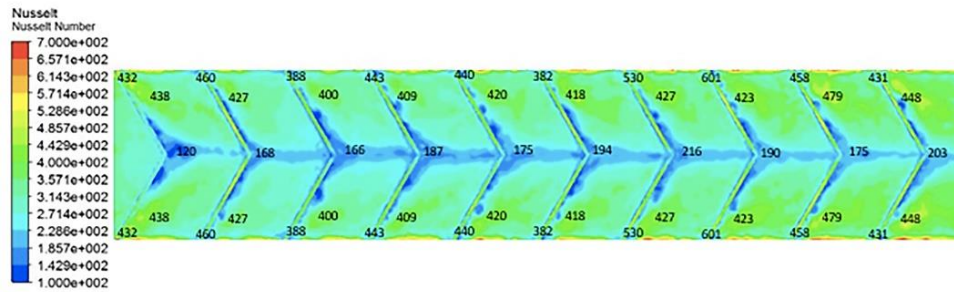
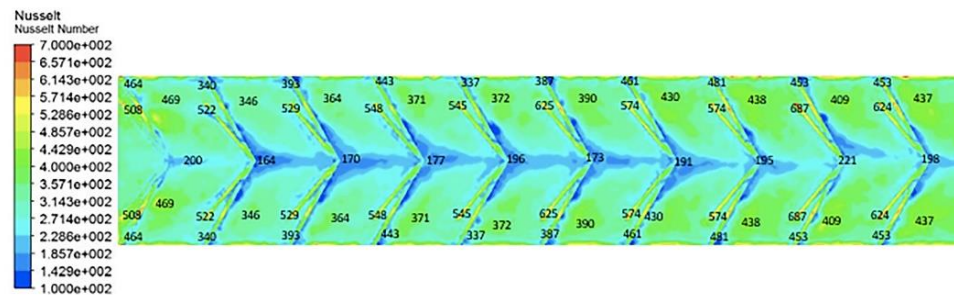
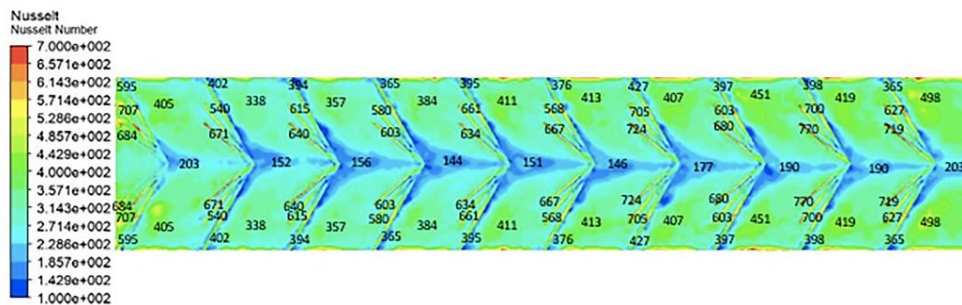
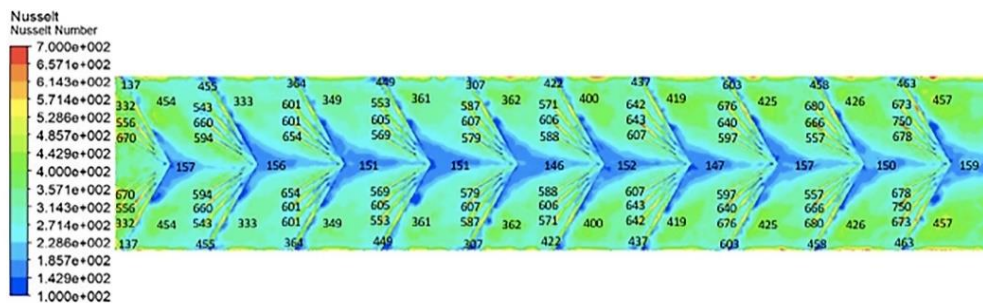
(a) V-down,  $B=2$ (b) V-down,  $B=4$ (c) V-down,  $B=6$ (d) V-down,  $B=8$ Figure 4. 21 Nusselt number contours for  $P/e=20$  and  $Re=86500$ .

Figure 4.21 shows the Nusselt number contours for V-ribs at  $P/e=20$  and  $Re=86500$ . These reflect the pressure contribution and the vorticity strength contours. The ribs' structure of its branches and particularly the tips are local maximum of heat transfer. The reattachment regions occupy the channel's broad expanses with medium heat transfer capacity. While, the recirculation zone mainly behind the ribs' apex has low heat transfer.

The effect of increasing the branching number adds obstacles in triggering flow turbulent motion near wall. In effect, for high relative pitch ratio, this goal has been achieved in incrementing heat transfer augmentation, particularly for  $B=6$  and  $8$ . However, with too much obstacles as in the case of  $B=8$ , zones of low circulation (Section 4.4.2) were broadened and the expanse of low heat transfer augmentation became a recoiled negative contribution on the overall heat transfer performance. V-ribs with  $B=6$  provides optimal overall heat transfer performance for the roughened channel with V-rib shape.

## CHAPTER 5

### CONCLUSION AND SUGGESTION FOR FUTURE WORKS

#### 5.1 Conclusion

This present study reports the effects of the heat transfer performance, the friction factor and the thermal hydraulic performance of the continuous V-ribs with varied branching number and pitch ratio placed only on the heated plate of a rectangular duct. The main conclusions are:

(1) Heat transfer of a smooth channel was significantly improved by application of V-ribs. The average Nusselt number and thermohydraulic performance of a smooth channel were raised by 108% and 39%, while the friction factor increased by 185%.

(2) Longitudinal co-rotating vortices as the main secondary flow induced by the continuous V-ribs.

(3) The relative pitch ratio serves to increase or decrease the number of reattachment points behind ribs. Low relative pitch ratio ( $P/e=10$ ) can allow too few reattachments to occur. While increasing the relative pitch ratio (to  $P/e \geq 15$ ) can optimize either the heat transfer performance or the thermal hydraulic performance. The optimal  $P/e$  for the heat transfer augmentation is  $P/e=20$ . The optimal  $P/e$  that improves the overall THP is  $P/e=15$ .

(4) For low relative pitch ratio ( $P/e=10$ ), increasing the branching number lowers both the heat transfer and the pressure drop of the channel. At higher relative pitch ratio ( $P/e \geq 15$ ), increasing the branching number has null effect on heat transfer and only lower the friction factor. At the pitch ratio of 10, increasing the branching number from 2 to 8 lowers the frictional loss by 23%. At the pitch ratio of 20, this reduction would be 12%.

(5) The branching number of 6 for the branched V-rib allowed optimal thermal hydraulic performance.

## 5.2 Suggestion for future works

It can be concluded that the V-rib model in application of the heat exchanger can be optimized such that the branching number of the rib is 6. Improvement for further experiments can be made by placing the ribs on opposite walls of the channel, designing the ribs with gaps and staggered piece, and using a multiple branched V-rib.



## REFERENCES

- [1] A. Kumar and M.-H. Kim, "Effect of roughness width ratios in discrete multi V-rib with staggered rib roughness on overall thermal performance of solar air channel," *Solar Energy*, vol. 119, pp. 399-414, 2015/09/01/ 2015.
- [2] A. Kumar, R. P. Saini, and J. S. Saini, "Experimental investigation on heat transfer and fluid flow characteristics of air flow in a rectangular duct with Multi v-shaped rib with gap roughness on the heated plate," *Solar Energy*, vol. 86, no. 6, pp. 1733-1749, 2012/06/01/ 2012.
- [3] V. Singh Bisht, A. Kumar Patil, and A. Gupta, "Review and performance evaluation of roughened solar air heaters," *Renewable and Sustainable Energy Reviews*, vol. 81, pp. 954-977, 2018/01/01/ 2018.
- [4] N. Zheng, P. Liu, Z. Liu, and W. Liu, "Numerical simulation and sensitivity analysis of heat transfer enhancement in a flat heat exchanger tube with discrete inclined ribs," *International Journal of Heat and Mass Transfer*, vol. 112, pp. 509-520, 2017/09/01/ 2017.
- [5] P. Promvong, W. Changcharoen, S. Kwankaomeng, and C. Thianpong, "Numerical heat transfer study of turbulent square-duct flow through inline V-shaped discrete ribs," *International Communications in Heat and Mass Transfer*, vol. 38, no. 10, pp. 1392-1399, 2011/12/01/ 2011.
- [6] M. S. Vázquez, W. V. Rodríguez, and R. Issa, "Effects of ridged walls on the heat transfer in a heated square duct," *International Journal of Heat and Mass Transfer*, vol. 48, no. 10, pp. 2050-2063, 2005/05/01/ 2005.
- [7] P. Singh, Y. Ji, and S. V. Ekkad, "Experimental and numerical investigation of heat and fluid flow in a square duct featuring criss-cross rib patterns," *Applied Thermal Engineering*, vol. 128, pp. 415-425, 2018/01/05/ 2018.
- [8] S. Alfarawi, S. A. Abdel-Moneim, and A. Bodalal, "Experimental investigations of heat transfer enhancement from rectangular duct roughened by hybrid ribs," *International Journal of Thermal Sciences*, vol. 118, pp. 123-138, 2017/08/01/ 2017.
- [9] R. K. Ravi and R. P. Saini, "Experimental investigation on performance of a double pass artificial roughened solar air heater duct having roughness elements of the combination of discrete multi V shaped and staggered ribs," *Energy*, vol. 116, pp. 507-516, 2016/12/01/ 2016.
- [10] L. Luo, F. Wen, L. Wang, B. Sundén, and S. Wang, "Thermal enhancement by using grooves and ribs combined with delta-winglet vortex generator in a solar receiver heat exchanger," *Applied Energy*, vol. 183, pp. 1317-1332, 2016/12/01/ 2016.
- [11] X. Daguene-Frick, A. Toutant, F. Bataille, and G. Olalde, "Numerical investigation of a ceramic high-temperature pressurized-air solar receiver," *Solar Energy*, vol. 90, pp. 164-178, 2013/04/01/ 2013.
- [12] M. Di Capua H, R. Escobar, A. J. Diaz, and A. M. Guzmán, "Enhancement of the cooling capability of a high concentration photovoltaic system using microchannels with forward triangular ribs on sidewalls," *Applied Energy*, vol. 226, pp. 160-180, 2018/09/15/ 2018.

- [13] A. Rezaia and L. A. Rosendahl, "Feasibility and parametric evaluation of hybrid concentrated photovoltaic-thermoelectric system," *Applied Energy*, vol. 187, pp. 380-389, 2017/02/01/ 2017.
- [14] A. R. Sampath, "Effect of Rib Turbulators on Heat Transfer Performance in Stationary Ribbed Channels," Cleveland State University, 2009.
- [15] V. S. Hans, R. P. Saini, and J. S. Saini, "Heat transfer and friction factor correlations for a solar air heater duct roughened artificially with multiple v-ribs," *Solar Energy*, vol. 84, no. 6, pp. 898-911, 2010/06/01/ 2010.
- [16] S. Singh, S. Chander, and J. S. Saini, "Heat transfer and friction factor correlations of solar air heater ducts artificially roughened with discrete V-down ribs," *Energy*, vol. 36, no. 8, pp. 5053-5064, 2011/08/01/ 2011.
- [17] H. Schlichting and K. Gersten, *Boundary-layer theory*, 8th rev. and enl. ed. Berlin ; New York: Springer, 2000, pp. xxiii, 799 p.
- [18] X. Gao and B. Sundén, "Heat transfer and pressure drop measurements in rib-roughened rectangular ducts," *Experimental Thermal and Fluid Science*, vol. 24, no. 1, pp. 25-34, 2001/03/14/ 2001.
- [19] H. Sturm, G. Dumstorff, P. Busche, D. Westermann, and W. Lang, "Boundary layer separation and reattachment detection on airfoils by thermal flow sensors," *Sensors (Basel, Switzerland)*, vol. 12, no. 11, pp. 14292-14306 Accessed on: 2012. doi: 10.3390/s121114292 Available: <http://europepmc.org/abstract/MED/23202160>  
<http://europepmc.org/articles/PMC3522913?pdf=render>  
<http://europepmc.org/articles/PMC3522913>  
<https://www.ncbi.nlm.nih.gov/pmc/articles/pmid/23202160/?tool=EBI>  
<https://www.ncbi.nlm.nih.gov/pmc/articles/pmid/23202160/pdf/?tool=EBI>  
<https://doi.org/10.3390/s121114292>
- [20] A. Andreozzi, O. Manca, S. Nardini, and D. Ricci, "Forced convection enhancement in channels with transversal ribs and nanofluids," *Applied Thermal Engineering*, vol. 98, pp. 1044-1053, 2016/04/05/ 2016.
- [21] R. Karwa, "EXPERIMENTAL STUDIES OF AUGMENTED HEAT TRANSFER AND FRICTION IN ASYMMETRICALLY HEATED RECTANGULAR DUCTS WITH RIBS ON THE HEATED WALL IN TRANSVERSE, INCLINED, V-CONTINUOUS AND V-DISCRETE PATTERN," *International Communications in Heat and Mass Transfer*, vol. 30, no. 2, pp. 241-250, 2003/03/01/ 2003.
- [22] S. C. Lau, R. T. Kukreja, and R. D. McMillin, "Effects of V-shaped rib arrays on turbulent heat transfer and friction of fully developed flow in a square channel," *International Journal of Heat and Mass Transfer*, vol. 34, no. 7, pp. 1605-1616, 1991/07/01/ 1991.
- [23] A.-M. Ebrahim Momin, J. S. Saini, and S. C. Solanki, "Heat transfer and friction in solar air heater duct with V-shaped rib roughness on absorber plate," *International Journal of Heat and Mass Transfer*, vol. 45, no. 16, pp. 3383-3396, 2002/07/01/ 2002.
- [24] G. Tanda, "Heat transfer in rectangular channels with transverse and V-shaped broken ribs," *International Journal of Heat and Mass Transfer*, vol. 47, no. 2, pp. 229-243, 2004/01/01/ 2004.

- [25] V. S. Hans, R. S. Gill, and S. Singh, "Heat transfer and friction factor correlations for a solar air heater duct roughened artificially with broken arc ribs," *Experimental Thermal and Fluid Science*, vol. 80, pp. 77-89, 2017/01/01/ 2017.
- [26] A. Kumar and M.-H. Kim, "Heat transfer and fluid flow characteristics in air duct with various V-pattern rib roughness on the heated plate: A comparative study," *Energy*, vol. 103, pp. 75-85, 2016/05/15/ 2016.
- [27] D. Lorenzini-Gutierrez, A. Hernandez-Guerrero, J. L. Luviano-Ortiz, and J. C. Leon-Conejo, "Numerical and experimental analysis of heat transfer enhancement in a grooved channel with curved flow deflectors," *Applied Thermal Engineering*, vol. 75, pp. 800-808, 2015/01/22/ 2015.
- [28] D. S. Thakur, M. K. Khan, and M. Pathak, "Solar air heater with hyperbolic ribs: 3D simulation with experimental validation," *Renewable Energy*, vol. 113, pp. 357-368, 2017/12/01/ 2017.
- [29] A. Kumar Rohit and A. Lanjewar, *Thermo-Hydraulic Performance Evaluation Using W-Discrete Rib in Solar Air Heater*. 2016.
- [30] P. Singh, B. V. Ravi, and S. V. Ekkad, "Experimental and numerical study of heat transfer due to developing flow in a two-pass rib roughened square duct," *International Journal of Heat and Mass Transfer*, vol. 102, pp. 1245-1256, 2016/11/01/ 2016.
- [31] D. Jin, M. Zhang, P. Wang, and S. Xu, "Numerical investigation of heat transfer and fluid flow in a solar air heater duct with multi V-shaped ribs on the absorber plate," *Energy*, vol. 89, pp. 178-190, 2015/09/01/ 2015.
- [32] A. Kumar, R. P. Saini, and J. S. Saini, "Development of correlations for Nusselt number and friction factor for solar air heater with roughened duct having multi v-shaped with gap rib as artificial roughness," *Renewable Energy*, vol. 58, pp. 151-163, 2013/10/01/ 2013.
- [33] S.-M. Lee and K.-Y. Kim, "Multi-objective optimization of arc-shaped ribs in the channels of a printed circuit heat exchanger," *International Journal of Thermal Sciences*, vol. 94, pp. 1-8, 2015/08/01/ 2015.
- [34] R. S. Gill, V. S. Hans, and S. Singh, "Investigations on thermo-hydraulic performance of broken arc rib in a rectangular duct of solar air heater," *International Communications in Heat and Mass Transfer*, vol. 88, pp. 20-27, 2017/11/01/ 2017.
- [35] R. S. Gill, V. S. Hans, J. S. Saini, and S. Singh, "Investigation on performance enhancement due to staggered piece in a broken arc rib roughened solar air heater duct," *Renewable Energy*, vol. 104, pp. 148-162, 2017/04/01/ 2017.
- [36] R. Nadda, A. Kumar, and R. Maithani, "Developing heat transfer and friction loss in an impingement jets solar air heater with multiple arc protrusion obstacles," *Solar Energy*, vol. 158, pp. 117-131, 2017/12/01/ 2017.
- [37] R. Nadda, R. Maithani, and A. Kumar, "Effect of multiple arc protrusion ribs on heat transfer and fluid flow of a circular-jet impingement solar air passage," *Chemical Engineering and Processing - Process Intensification*, vol. 120, pp. 114-133, 2017/10/01/ 2017.
- [38] R. W. Fox and A. T. McDonald, *Introduction to fluid mechanics*. Wiley, 1985.
- [39] D. C. Wilcox, *A half century historical review of the k-omega model*. 1991.

- [40] *ANSYS FLUENT Theory Guide*. 2011.
- [41] T. L. Bergman, F. P. Incropera, A. S. Lavine, and D. P. DeWitt, *Introduction to Heat Transfer*. Wiley, 2011.
- [42] N. S. Deo, S. Chander, and J. S. Saini, "Performance analysis of solar air heater duct roughened with multigap V-down ribs combined with staggered ribs," *Renewable Energy*, vol. 91, pp. 484-500, 2016/06/01/ 2016.







จุฬาลงกรณ์มหาวิทยาลัย  
**CHULALONGKORN UNIVERSITY**

## VITA

**NAME** Warissara Tangyotkhajorn

**DATE OF BIRTH** 28 March 1990

**PLACE OF BIRTH** Bangkok, Thailand

**INSTITUTIONS ATTENDED** Bachelor of Science in Physics and Mathematics, 2014.  
The University of St Andrews--St Andrews, Fife, Scotland.  
Thesis/Dissertation: A very brief introduction on turbulence.  
Ruamrudee International School, 2009--Bangkok, Thailand

**HOME ADDRESS** 19/9 M.4 Watcharapol Rd., Klongtanon, Saimai, Bangkok, Thailand, 10220



จุฬาลงกรณ์มหาวิทยาลัย  
CHULALONGKORN UNIVERSITY